Functional role of respiratory supercomplexes in mice: segmentation of the Q_{pool} and SCAF1

Enrique Calvo[1†], Sara Cogliati[1,2†], Pablo Hernansanz-Agustín[1†], Marta Loureiro-López[1†], Adela Guarás[1], Rafael A. Casuso[2], Fernando García-Marqués[1], Rebeca Acín-Pérez[1], Yolanda Martí-Mateos[1], JC. Silla-Castro[1], Marta Carro-Alvarellos[1], Jesús R. Huertas[2], Jesús Vázquez[1,3*] and J.A. Enríquez[1,4*]

[1] Centro Nacional de Investigaciones Cardiovasculares Carlos III. Madrid 28029, Spain.

[2] Institute of Nutrition and Food Technology, Biomedical Research Centre, Department of Physiology, University of Granada

[3] CIBERCV, Madrid, Spain

[4] CIBERFES, Madrid, Spain

*Correspondence to: J. Vázquez (jvazquez@cnic.es) or J.A. Enríquez (jaenriquez@cnic.es)

† these four authors contributed equally.

Summary

Mitochondrial respiratory complexes assemble into different forms of supercomplexes (SC). In particular, SC III_2+IV require the SCAF1 protein. However, the structural role of this factor in the formation of the respirasome ($I+III_2+IV$) and the physiological role of SCs are controversial. Here, we study C57BL/6J mice harbouring either non-functional SCAF1, the full knock-out for SCAF1 or the wild-type version of the protein and found a growth and exercise phenotype due to the lack of functional SCAF1. By combining quantitative data-independent proteomics, high resolution 2D Blue Native Gel Electrophoresis and functional analysis of enriched respirasome fractions, we show that SCAF1 confers structural attachment between III_2 and IV within the respirasome, increases NADH-dependent respiration and reduces ROS production. Furthermore, through the expression of AOX in cells and mice we confirm that CI-CIII superassembly segments the CoQ in two pools and modulates CI-NADH oxidative capacity. These data demonstrate that SC assembly, regulated by SCAF1, modulates the functionality of the electron transport chain.

Introduction

The mitochondrial cristae are the main site of biological energy conversion through the respiratory complexes I to V known as oxidative phosphorylation system (OXPHOS). Our understanding of the structure of the mitochondria electron transport chain was shaken in 2000 by Herman Schägger when proposing that respiratory complexes could form superstructures called supercomplexes (SCs), among which the ones containing CI, CIII and CIV were named respirasomes (Schagger, 2000). This proposal came from a novel electrophoretic methodology mastered by that author named Blue Native Gel Electrophoresis (BNGE). First received with extreme skepticism, SCs are nowadays generally accepted as true biological entities. They are present in mitochondria from very different sources (Eubel et al., 2003; Schägger, 2002); they are able to respire (Acín-Pérez et al., 2008); specific factors for the formation of some SCs have been discovered (Lapuente-Brun et al., 2013); and the cryo-electron microscopy structures of the respirasome ($I+III_2+IV$) and the supercomplex $I+III_2$ have been obtained (Gu et al., 2016; Letts

2

52   et al., 2016; Sousa et al., 2016). Although all these data demonstrate their existence, the

53   physiological role of SCs is still under strong debate. A line of thinking proposes that SCs have

54   no functional role (Milenkovic et al., 2017). Other authors indicate that SCs optimize electron

55   flux to gain efficiency in energy generation while minimizing reactive oxygen species production

56   (Lapuente-Brun et al., 2013; Lenaz and Genova, 2007; Maranzana et al., 2013). We proposed the

57   "Plasticity Model", where individual and super-assembled complexes coexist in a regulated

58   equilibrium within the inner mitochondrial membrane (Acín-Pérez et al., 2008; Enríquez, 2016).

59   Thus, SCs rearrange in response to a shift in the metabolic source of electrons (Guarás et al.,

60   2016), in the metabolic adaptation of specialised cells in vivo (Garaude et al., 2016), or to adapt

61   the cell to different nutrients and physiological conditions (Greggio et al., 2017; Lopez-Fabuel et

62   al., 2016). For instance, under starvation the preferential use of fatty acids reduces the levels of

63   SCs containing CI, so that free III_2 is more accessible to electrons coming from $FADH_2$

64   (Lapuente-Brun et al., 2013).

65   The controversy was centered in the biological role of SCAF1 in respirasomes and in the

66   role of SCs in the functional segmentation of the CoQ pool. In mouse, SCAF1 is 113 amino acid

67   long and has a high homology in its carboxy terminus with one subunit of CIV, for which there

68   are two isoforms (COX7A1- 80 aa and COX7A2- 83 aa). The amino-terminal portion of the

69   protein has no homology with any known protein. SCAF1 is required to super-assemble CIII and

70   CIV by replacing COX7A2 in the structure of CIV and by binding CIII through its amino-terminal

71   portion (Cogliati et al., 2016). Interestingly, all inbred mouse C57BL/6 sub-strains investigated

72   to date (Enríquez, 2019), harbor a non-functional version of SCAF1 (named SCAF1[111]) that, due

73   to a microdeletion that eliminate two amino acids, is unable to interact with CIV (Cogliati et al.,

74   2016). In the absence of functional SCAF1, the SC III_2+IV and the majority of SCs containing

75   CI, CIII and CIV cannot be formed (Cogliati et al., 2016; Lapuente-Brun et al., 2013; Lobo-Jarne

76   et al., 2018). However, in some instances, particularly in heart mitochondria from BL/6 mice, a

77   comigration between CI, CIII and CIV suggestive of the presence of respirasomes can be observed

78   (Cogliati et al., 2016; Lobo-Jarne et al., 2018). This raised doubts about the relevance of SCAF1

79   for the formation and function of the respirasome (Lobo-Jarne et al., 2018). In addition, we

3

80   observed, confirming the previous suggestions (Bianchi et al., 2004), that superassembly partially

81   segments CoQ in two pools, one predominantly dedicated to FAD and another to NAD(Lapuente-

82   Brun et al., 2013). Noteworthy, these data were obtained using isolated mitochondria. Elsewhere,

83   but using sub-mitochondrial particles, opposite conclusions were reported (Fedor and Hirst,

84   2018), calling the partial CoQ partitioning hypothesis into question.

85   In this work we demonstrate that the ablation of SCAF1 decreases the performance of

86   mice under rigorous metabolic stresses such as reduced food supply or intense exercise demand.

87   In addition, by combining data-independent proteomics, 2D BNGE-based structural analysis and

88   functional studies of the BNGE enriched respirasome fractions, we demonstrate that SCAF1 plays

89   a key role in the regulation of the structure of respirasome and its bioenergetics performance. In

90   addition, through the expression of AOX in several cell systems and animals, we have been able

91   to confirm the segmentation of the CoQ in two pools is a consequence of the superassembly

92   between CI and CIII. These findings demonstrate that SCs play a physiological role and provide

93   a molecular mechanism for the phenotype observed in animals.

94   **Results**

95   **The ablation of functional SCAF1 compromises growth under food restriction and impairs**

96   **exercise performance.**

97   One of the more recurrent arguments to challenge the proposal that SCAF1 and the

98   superassembly between complexes III and IV are bioenergetically relevant is the belief that all

99   C57BL/6 mice sub-strains, which harbor a non-functional SCAF1, lack an apparent phenotype.

100   Since this belief has never been experimentally addressed, we first investigated it in detail. We

101   compared the phenotype of C57BL/6 mice with full ablation of SCAF1 ($SCAF1^{-/-}$ or $SCAF1^{KO}$),

102   with the non-functional version of SCAF1 ($SCAF1^{111/111}$), and with the wild-type and functional

103   version of this gene in homozygosis ($SCAF1^{113/113}$). We first confirmed that $SCAF1^{113/113}$ liver

104   and heart mitochondria express high levels of SCAF1 that are associated substantially with the

105   respirasome and SC: III_2+IV (Fig. 1A). On the other hand, and as described before (Cogliati et

106   al., 2016), $SCAF1^{111}$ was very unstable and could only be found in minor amounts, interacting

107   with CIII either in the I+III_2 or in III_2 (Fig. 1A). In the full KO mice, no SCAF1 could be detected

4

108   (Fig. 1A). Work from our group revealed that the ablation of SCAF1 in zebrafish affects the

109   growth of male and female animals, the female fertility and the swimming performance of

110   otherwise healthy animals. We also showed that all these phenotypic features disappear when

111   overfeeding the animals (García-Poyatos et al., 2019). Therefore, we hypothesized that since in

112   the usual food regime of mouse facilities animals are fed ad-libitum, a situation that can be

113   considered overfeeding, C57BL/6 mice would be protected against similar manifestations of the

114   lack of functional SCAF1. Therefore, we first evaluated if the presence of functional SCAF1 in

115   mice had any physiological impact under restricted food administration. Animals were feed ad

116   libitum for 24 hours every three days and were fasted during the rest of the time (Fig. 1B). During

117   the first days the animals suffered a period of adaptation in which SCAF1^{113} males were able to

118   maintain or even increase their weight, whereas SCAF1^{111} and KO males showed the opposite

119   trend (Fig. 1C). This period also resulted in the loss of some mice, without significant differences

120   between strains but with a clearly better survival rate of females vs. males (Fig. S1A). Once

121   adapted, all animals started gaining weight. These results indicate that the absence of SCAF^{113}

122   affects mice physiology and that SCAF^{111} does not retain any significant functionality (Fig. 1C).

123   Interestingly, females were insensitive to the presence of functional SCAF1 (Fig. 1C), probably

124   due to a different female mechanism of adaptation to fasting (Della Torre et al., 2018). Next, we

125   evaluated the impact of functional SCAF1 on exercise performance. Thus, we found that both

126   male and female SCAF1^{113} were able to reach a 30% higher maximum speed in the treadmill than

127   any other group of animals (Fig. 1D). These studies demonstrate that the presence of functional

128   SCAF1 has a direct impact on the mice phenotype, implying that supercomplex formation allows

129   a more efficient electron transport chain. This increased efficiency allows males to better extract

130   energy from aliments, and both sexes to respond to higher muscle work demands. The observation

131   that SCAF1 ablation causes such evident phenotype demands a deeper look into the molecular

132   role of this protein in the function of the mitochondrial electron transport chain, which could help

133   to solve the controversy on this issue. To that aim, we combined unbiased complexome analysis

134   by mass spectrometry, 2D-BNGE evaluation of the interaction of respiratory complexes within

5

135   supercomplexes, and functional analysis of enriched fractions of complexes and supercomplexes

136   in the presence or in the absence of functional SCAF1.

137   **The size distribution of OXPHOS components is tissue-specific as a consequence of**

138   **superassembly**

139   First, we applied Blue-DiS, a recently developed technology that takes advantage of the

140   reproducibility and sensitivity of data-independent mass spectrometry(Guarás et al., 2016), to

141   perform mitochondrial complexome profiling from a completely hypothesis-free perspective.

142   Thus, mitochondria-enriched preparations from heart, brain and liver from CD1 mice and from

143   the cell line L929 repopulated with mtDNA from C57BL/6mice (L929^{C57}), having all of them the

144   wild type functional version of SCAF1, were separated by BNGE and each lane was cut into 26

145   slices; each slice was subjected to trypsin protein digestion and analyzed by MS using the DiS

146   method we previously developed (Guarás et al., 2016). We identified 1,134 proteins classified as

147   mitochondrial in the Mitocarta 2.0 (Calvo et al., 2016), which correspond to 98% of all Mitocarta

148   annotated proteins (Fig. S1B). Mitochondrial enrichment was different between samples, being

149   heart (81% of peptide identifications annotated in Mitocarta) and liver (71%) more enriched in

150   known mitochondrial proteins; while brain showed a lower enrichment (38%) (Fig. S1C). In all

151   cases an almost complete coverage of components of OXPHOS complexes was achieved (Dataset

152   1). Every subunit from CII and CIII was identified (Fig. S1D), together with 41 out of the 44

153   annotated proteins from CI (Fig. S1D). Concerning CIV, this complex is built out of 14 proteins

154   but several of them have isoforms making up a total of 21 possible components. However,

155   COX6B2 and COX7B2 are both expressed only in sperm, and COX4i2 only in lung, so that 18

156   proteins were potentially identifiable in our samples, from which we detected 16 (Fig. S1D).

157   Regarding CV, we could detect 17 out of the 20 structural proteins of this complex (Fig. S1D).

158   Apparent molecular weights could be accurately assigned to each one of the 26 BNGE slices from

159   the known masses of individual complexes and of SC (Fig. S1E).

160   We performed a cross-correlation analysis of protein abundances across different slices

161   within the same mitochondrial type (Fig. S2A). This analysis showed that the relative abundances

162   of all proteins belonging to either CI, CIII, CIV or CV were constant across slices (Fig. S2A &

6

163   Supplementary Table 1), and that the most representative slice from each complex also had the

164   same protein proportions across the different mitochondrial types (Fig. S2B & Supplementary

165   Table 2). In striking contrast, the electrophoretic mobility protein distributions of CI, CIII and

166   CIV, but not of CV, were markedly different from one mitochondrial source to another (Fig. S2C,

167   D). Thus, complexes in different tissues have the same protein composition but form tissue-

168   specific high molecular weight structures.

169   Notably, the larger structures (slides 1-8) consistently contained identical proportions of

170   CI and CIII, or CIII and CIV proteins (Fig. 2A, B). Cross correlation analysis confirmed that the

171   protein composition in the I+III+IV, I+III and III+IV structures was maintained between the

172   adjacent slices (Fig. 2C) and between tissues (Fig. 2D), reflecting the formation of SC in an

173   unbiased manner. To obtain a quantitative estimate of the distribution of these structures in each

174   tissue we modelled the complete migration profiles of CI, CIII and CIV by unsupervised gaussian

175   deconvolution. We found that in all mitochondrial types the profile of CI and CIII could be

176   accurately explained as a superimposition of broad gaussian peaks corresponding to a ternary

177   complex (I+III+IV), to binary I+III and III+IV structures and to free CI, CIII and CIV forms

178   (dashed red lines in Fig. 2E and Fig. S2D), having these components the same electrophoretic

179   mobilities and similar peak widths across all mitochondrial sources (Fig. 2F). We also found that

180   the profile of CIV could not be adequately explained by these structures around slices 6-12 (Fig.

181   2E, black arrows), suggesting the presence of significant amounts of CIV dimers and multimers.

182   Thus, the addition of two more CIV structures (IV_2 and IV_m) was sufficient to model the migration

183   profile of this complex in all mitochondrial types (dashed red lines in Fig. 2E and Fig. S2D).

184   To further validate the predicted structures of OXPHOS molecular assemblies, we

185   performed a Blue-DiS analysis of mitochondria from cultured mutant cell lines that are unable to

186   assemble one or more of the complexes (Diaz et al., 2006; Moreno-Loshuertos et al., 2006;

187   Perales-Clemente et al., 2010). In the cell line ΔCI , which lacked the ND4 subunit from CI and

188   was unable to assemble CI (Moreno-Loshuertos et al., 2006), neither free CI nor SCs $I+III_2$ and

189    $I+III_2+IV$ could be detected (Fig. S3A, B); however, free III_2 and IV and the SC III_2+IV were

190   detected at the expected sizes (green rectangles). In the case of the mutant cell line for Cox10

7

191 protein (ΔCIV), which lacks assembled CIV, all structures containing CIV were absent (red

192 rectangles in Fig. S3A, B). In addition, the structures containing CI could neither be detected, in

193 agreement with the fact that CIV is needed for the stabilization of CI (Diaz et al., 2006); hence in

194 this mutant only the free III_2 form was detectable (green rectangles in Fig. S3A, B). Finally, in

195 the Rho 0 cell line, which lacks mitochondrial DNA encoding for different subunits of the

196 respiratory complexes, none of these structures were observed (red rectangles in Fig. S3A).

197 However, CII, which is totally encoded in the nucleus, and a CV form of smaller size (V*)

198 remained detectable in these cells (Fig. S3A).

199   In summary, the complete size distributions of OXPHOS components could be explained

200 by structures of constant size and composition that were present in each mitochondrial type at

201 different relative proportions (Fig. 2F).

202 **Respiratory complexes are assembled into supercomplexes at fixed stoichiometries.**

203   The notion that SC contained complexes at fixed stoichiometries was reinforced by the

204 finding that the protein composition of SC was conserved in all mitochondrial types (Fig. 2D).

205 We took advantage of the good linear response of quantitative Blue-DiS protein values (Fig. 2A,

206 B; Fig. S2A) to estimate the relative molar stoichiometries of complexes within each slice (Fig.

207 S3C, D, see M&M for detailed explanation). From slices 2 to 6 the relative molar proportion

208 CIII:CI was 2:1, in the four mitochondrial types, implying that the proportion $I+III_2$ is constant in

209 the respirasome and in the SC formed by CI and CIII (Fig. S3E). Besides, the relative molar

210 proportions CI:CIV and CIII:CIV were 1:1 and 2:1, respectively, between slices 2 to 4, implying

211 that the respirasome has a composition $I+III_2+IV$ (Fig. S3E).

212   To our knowledge, these are the first stoichiometry estimations of OXPHOS complexes

213 made by mass spectrometry, which agree with the structures analysed by cryo-electron

214 microscopy (Gu et al., 2016; Letts et al., 2016; Sousa et al., 2016), and contradict the

215 experimentally unsupported, but generalized tendency to assume that there are multiple types of

216 respirasomes that differed in their increasing content of 1-4 CIV monomers. The reason for the

217 split of the respirasome in several discrete bands in BNGE, corresponding to a broad peak in

218 Blue-Dis analysis, remains to be clarified. In slices 5 and 6, CIV is still detected although at a

8

219   lower proportion, suggesting that in this area migrate CIV superstructures of unknown

220   composition (Fig. 3E). Slices 7 and 8 are enriched in CI, where it migrates as a free complex, but

221   again with significant presence of CIV in different high molecular weight structures. Finally, the

222   relative proportions of CIII and CIV in bands 9 and 10 are coherent with a stoichiometry 2:1 (SC:

223   III_2+IV) (Fig. 3E). In summary, unbiased Blue-DiS analysis reinforces the results obtained by

224   other techniques and provide complementary evidence that OXPHOS complexes are arranged

225   into SC at fixed stoichiometries.

226   **CIV forms novel supercomplexes**

227   Our complexome analysis predicts that several structures that contain CIV, not yet

228   molecularly characterized, should be present. These are CIV structures above and below SC:

229   III_2+IV but also some CIV structures of higher molecular weight migration around $I+III_2$ and

230   $I+III_2+IV$. The existence IV_2 is well documented, and high molecular weight entities containing

231   only CIV have been described elsewhere (Cogliati et al., 2016). To confirm whether the CIV

232   structures predicted by Blue-DiS analysis are true entities, we performed 2D-BNGE of CD1 heart

233   mitochondria using in the first dimension digitonin as detergent to preserve the integrity of

234   supercomplexes and n-Dodecyl-β-D-maltoside (DDM) in the second dimension to disaggregate

235   supercomplexes into their component complexes. This procedure partially preserves the

236   interaction between CIII and CIV and the IV_2 (Perales-Clemente et al., 2010). As shown in Fig.

237   3A this analysis confirmed the presence of IV_2 and two forms of CIV that migrate immediately

238   faster and slower than SC III_2+IV and that do not super-assemble with any other respiratory

239   complex (IVm and IVn in Fig. 3A). These three structures account for a significant proportion of

240   the CIV in heart samples. In addition, we detected the presence of low proportions of a putative

241   SC: $I+IV_2$, which migrates with SC $I+III_2$ and segregates into CI and dimer CIV (Fig. S3F), and

242   of a putative SC I+IV, which migrates between free CI and SC: $I+III_2$ (Fig. S3F).

243   More surprisingly, we found CI and CIV monomer but without CIII that migrate between

244   SC: $I+III_2+IV$ and SC $I+III_2$, very close to the faster migrating respirasome band $I+III_2+IV$ (Fig.

245   S3F, labelled as I+IV?). The reason why this putative SC migrates with the apparent molecular

246   weight of a respirasome is unclear and may indicate that this structure interacts with a yet to

247   discover mitochondrial inner membrane component. Therefore, 2D-BNGE analysis of heart

248   mitochondria reveals specific supercomplexes that contain CIV, confirming Blue-DiS

249   predictions, and also CIV and CI together and that need to be further investigated. Note that, due

250   to their relatively low abundances, these additional IV structures are fully compatible with the

251   gaussian models of CI and CIV determined from Blue-DiS profiles.

252   **SCAF1 confers structural attachment between III$_2$ and IV within the respirasome**

253   To identify potential interaction partners of specific SC structures from the Blue-DiS

254   analysis, we generated their reference migration profiles *in silico* by combining the SC profiles

255   obtained by deconvolution analysis and performing a correlation search for all identified proteins

256   displaying a similar profile. This analysis led to a natural, hypothesis-free detection of

257   Cox7a2l/SCAF1 as the only candidate showing a significant correlation in all the mitochondrial

258   types with the structures containing CIII and CIV together (ED Fig. 4a left & b). Consistently,

259   deletion of CI inhibited the migration of SCAF1 in the position of the respirasome, but not in the

260   position of SC III$_2$+IV, and no traces of SCAF1 were detected in the mutant lacking CIV or in

261   Rho 0 cells (Fig. S4A right). These results obtained by unbiased complexome analysis provide

262   further experimental evidence that this protein regulates the interaction between these complexes,

263   as we postulate in previous reports (Cogliati et al., 2016; Lapuente-Brun et al., 2013).

264   Next, we analyzed by gaussian deconvolution the Blue-DiS profiles of mitochondria

265   prepared from SCAFI[111] heart and liver C57BL/6JOlaHsd mitochondria. As shown in Fig. 3B, in

266   BL6 liver the peaks corresponding to the respirasome and the SCs III$_2$+IV disappeared, while the

267   rest of structures, including SCs I+III$_2$ and the III$_2$ peaks, were maintained. However, while SC

268   III$_2$+IV was neither observed in BL6 heart, the presence of the respirasome remained clearly

269   detectable in this tissue (Fig. 3B). Therefore, BL6 and CD1 respirasomes are present in heart

270   mitochondria, but differ in the absence of SCAF1 in the former.

271   We reasoned that if the role of SCAF1 is to physically link CIII and CIV, and this function

272   is maintained in the respirasome, then mitochondria harboring SCAF1[113] and SCAF1[111] should

273   have different types of respirasomes differing structurally in the interaction between CIII and

274   CIV. To experimentally evaluate this hypothesis, we took advantage of the fact that upon 2D-

275   BNGE analysis the second dimension used to disaggregate supercomplexes (which employs

276   DDM) does retain significant amounts of the III_2+IV association, allowing us to discern whether

277   CIII and CIV are physically linked or not in the respirasome in the absence of functional SCAF1.

278   We performed 2D-BNGE with liver mitochondria derived from CD1, C57BL/6JOlaHsd mice and

279   also from C57BL/6JOlaHsd harboring the wild type version of SCAF1 (SCAF1[113]) generated in

280   our laboratory (Cogliati et al., 2016). This approach confirmed again that heart mitochondria from

281   BL6 mice does not assemble SC III_2+IV (Fig. 3C) and clearly demonstrated that the III_2+IV

282   structure remains within the respirasomes containing functional SCAF1 (CD1 and SCAF1[113]) but

283   not in those with the non-functional form (BL6[111]) (Fig. 3C). In conclusion, this analysis

284   demonstrates that SCAF1^{+} and SCAF1^{-} respirasomes are structurally different (Fig. 3D).

285   **SCAF1 enhances respiratory performance and reduce ROS production by the respirasome.**

286   We then inquired if the structural difference linked to the presence of an active SCAF1

287   form in the respirasome has any impact on their respiratory capacity. We first evaluated the

288   suitability to perform these kinetic analyses by confirming in isolated individual complexes (I,

289   III_2 and IV) that it is possible to measure the rate of oxidation and reduction of their respective

290   donor/acceptor of electrons and that they generate the expected stoichiometries. All the rates of

291   the individual complexes were similar regardless the strain of origin, with the exception of a mild

292   reduction in CIII activity in BL6[113] (Fig. S4C-E). Next, we excised BNGE bands containing SC

293   I+III_2+IV (respirasome) from SCAF1[113] (CD1, BL6[113] and 129 mice) and SCAF1[111] (C57BL/6J

294   mice) heart mitochondria and determined their respiratory capacity using NADH as substrate in

295   a Clark electrode (Acín-Pérez et al., 2008) and their NADH oxidation capacity by

296   spectrophotometry (Fig. 4A). For normalization purposes we determined the respiration capacity

297   induced by TMPD in the same samples after inhibition with antimycin and rotenone; we also

298   normalized by the protein content determined after eluting the respirasome from the gel. We found

299   that both SCAF1^{+} and SCAF1^{-}-containing respirasomes were able to perform NADH-dependent

300   respiration without the need of adding either external CoQ or Cyt c (Fig. 4B). Interestingly, the

301   respiratory capacity of the respirasome was much lower than that of CIV-monomer and NADH

302   oxidation was also decreased in comparison to that of CI. These results suggest, in agreement

11

303   with a recent observation on amphipol-stabilized SC:I+III$_2$, that superassembly of respiratory

304   complexes modulate their activity (Letts et al., 2019). Moreover, the rate of respiration by

305   SCAF1$^+$ respirasomes of different sources was about one order of magnitude higher than that of

306   the SCAF1$^-$ ones regardless of whether they are normalized by CIV-dependent respiration (Fig.

307   4C) or by protein content (Fig. 4D). In agreement with this observation, the rate of NADH

308   oxidization by SCAF1$^+$ respirasomes was between 3 and 4 times higher (Fig. 4E).

309   Lenaz's laboratory showed by reconstruction in liposomes that the association between

310   CI and CIII into SCs reduces the production of ROS (Maranzana et al., 2013). This observation

311   was validated in vivo by others (Lopez-Fabuel et al., 2016)·(Huertas et al., 2017). The availability

312   of respirasomes with different degree of interaction between III$_2$ and IV allowed us to investigate

313   whether this interaction impacts on the production of ROS. For this purpose, we incubated the

314   BNGE-excised respirasome bands from CD1, BL6^{S111} and BL6^{S113} heart mitochondria

315   preparations in the presence of NADH and Amplex-red to monitor ROS production. We found

316   no differences in the level of ROS produced by the respirasomes from any of the investigated

317   strains (Fig. 4F, G). Considering that the rate of respiration and NADH oxidation of SCAF1^{111}

318   respirasome is lower than its wild type counterpart, we calculated that the respirasome harbouring

319   the mutant version of SCAF1 derived 0,185% of NADH electrons to ROS, whereas CD1 and

320   SCAF1^{113} derived 0,064 % and 0,067%, respectively. Next, we repeated the experiment but

321   substituting NADH by CoQ$_1$H$_2$ to donate electrons to CIII and in the presence of rotenone to

322   block CI interaction with CoQ. Under these conditions, which mimic a stress situation with an

323   abnormal rise in CoQH$_2$, SCAF1$^-$ respirasomes produced significantly more ROS (Fig. 4F, G). In

324   all cases, ROS production was fully quenchable by the addition of superoxide dismutase and

325   catalase (Fig. 4F, G). Therefore, SCAF1$^+$ respirasomes produced less ROS than SCAF1$^-$ ones.

326   In summary, although SCAF1 can be dispensable for the formation of respirasomes it

327   confers structural attachment between complexes III$_2$ and IV within the respirasomes providing

328   more stability, significantly better functional performance and lower ROS production.

329   **Respiratory supercomplexes are unstable upon mitochondrial membrane disruption.**

330   The existence of two structurally distinct respirasomes was described recently in

331   ovine(Letts et al., 2016) and confirmed later in bovine models (Sousa et al., 2016). One form of

332   respirasome has complexes III_2 and IV tightly attached (named *tight respirasome*), while the other

333   is characterized by an increased distance between them (named *loose respirasome*). Our

334   observation that SCAF1 determines the interaction between III_2 and IV within the respirasome is

335   reminiscent of the existence of tight and loose respirasomes. Noticeably, both ovine and bovine

336   SCAF1 sequences match the mouse wild-type and functional 113 version.

337   Very intriguingly, Letts and co-workers observed that the proportion between both

338   respirasome forms in a given preparation is not stable. In fact, after incubation at 4º C the tight

339   respirasomes were transformed into the loose ones (Letts et al., 2016). We wondered whether this

340   phenomenon could be observed by BNGE analysis. Thus, we compared CD1-liver mitochondria

341   (which harbors the functional SCAF1 form), maintained several hours in the refrigerator, before

342   and after solubilization with digitonin. To our surprise, both SCs $I+III_2+IV$ and III_2+IV, but not

343   SC $I+III_2$, disappeared in the samples maintained at 4 ºC only if they were previously digitonized

344   (Fig. 5A). In addition, SCAF1 migrated as a bulk with the free CIV in the digitonized preparations

345   (Fig. 5A, B). Furthermore, 2D-BNGE/SDS-PAGE analysis revealed that the form of SCAF1 that

346   migrated with free CIV (marked with an asterisk) had a smaller molecular weight than the

347   canonical form (Fig. 5C). Proteomic analysis demonstrated that in slices corresponding to SC

348      $I+III_2+IV$, IV_2 and IV, a peptide spanning the sequence SSVTAYDYSGK (originated from the

349   corresponding SCAF1-derived tryptic peptide LTSSVTAYDYSGK) was unequivocally

350   identified exclusively in the non-fresh samples (Fig. 5E and Fig. S5A). This sequence was mapped

351   into the N-terminus region of the protein, which contains the CIII-interacting domain(Cogliati et

352   al., 2016) (underlined sequence in Fig. 5D). Further quantitative analysis revealed the coexistence

353   of the intact and proteolyzed forms of the peptide bound to CIV in the respirasome, while SC:

354   III_2+IV contained only the intact form (Fig. 5E). These results indicate that SCAF1 suffers a

355   partial proteolytic processing that disrupts SC: III_2+IV, destabilizes the respirasome and parallels

356   the loss of CIV-containing SCs. In silico analysis of the processing site in SCAF1 revealed a

357   putative cleavage site for calpain-1 (Fig. 5D). In agreement with this prediction the use of calpain

13

358   inhibitors was sufficient to prevent the cleavage of SCAF1 (Fig. 5F) and also to preserve the

359   integrity of CIV-containing SC after digitonin treatment (Fig. 5G). When similar experiments

360   were repeated with mitochondrial samples purified from CD1-heart we also observed the

361   relocation of SCAF1 with free CIV, but the reduction in the amount of CIV-containing SC was,

362   although evident, much milder (Fig. 5H). All these results indicate that SC are unstable or can

363   shift from tight (e.g. kinetically active) to loose (e.g. kinetically restrained) forms when

364   mitochondrial membrane integrity is compromised, likely as a consequence of the release of

365   proteases, such as calpain-1, and lipases that gain access to the inner mitochondrial membrane

366   and to the respiratory complexes.

367   It remains to be elucidated whether SCAF1 processing by calpain-1 is just an in vitro

368   artifact or a biologically relevant mechanism regulating SCs turnover dynamics. However, the

369   observation that respiratory complexes become unstable when the mitochondrial membrane

370   integrity is disrupted, raises serious concerns on the interpretation of the various published

371   experimental approaches used to investigate the function of the SCs. They include sub-

372   mitochondrial particles, where functional measurements were performed at 32 ºC (Blaza et al.,

373   2014; Fedor and Hirst, 2018); isolated mitochondria, which were incubated at 37 ºC (Guarás et

374   al., 2016; Lapuente-Brun et al., 2013); and partially isolated respirasomes (this report). To further

375   study this issue, we subjected digitonized and intact mitochondria from liver (Fig. S5B) and heart

376   (Fig. S5C) preparations to prolonged incubations at different temperatures. Liver digitonized

377   mitochondria completely lost the respirasome and the SC III$_2$+IV, after 72 hours at 4 ºC, and all

378   SCs, including I+III$_2$ after 3h at 37 ºC (Fig. 5A and Fig. S5B). Respirasomes from heart

379   digitonized mitochondria were more stable than those from liver at 4 ºC (72h) but were completely

380   lost after 3h at 37 ºC; at this temperature the SC III$_2$+IV and even the CIV monomer disappeared

381   (Fig. S5C). In contrast, all of these structures remained stable in intact organelles (Fig. S5B, C).

382   More worrying is the fact that the stability of both heart and liver SCs is not maintained if

383   digitonized mitochondria are incubated at 37 ºC for just one hour (Fig. S5D). All these

384   observations call to caution when performing experiments in disrupted mitochondria. Very

385   importantly, the differential stability of SC in intact and broken mitochondria may well be the

14

386   cause of the apparently discrepant results regarding the physiological role of respiratory

387   supercomplexes between different groups.

388   Our unexpected results prompted us to evaluate if BNGE purified respirasomes were

389   stable enough during functional studies to trust the conclusions presented above. To address this

390   issue, we kept the first-dimension gel for 1 or 3 hours at 37ºC after running the BNGE to inquire

391   if the respirasomes are preserved. After the incubation period we ran a second-dimension

392   electrophoresis also in the presence of digitonin to determine the intactness of structures, since

393   complexes and SCs are expected to migrate forming a diagonal unless some associations are

394   disrupted during incubation. Thus, after 1- or 3-hour incubation at 37 ºC the respirasome and any

395   other detected complex or SCs remained substantially intact apart from comet tail-like shape of

396   the spots due to diffusion in the 1st dimension gel during the long period of incubation (Fig. S5E).

397   Moreover, 2D-BNGE analysis, using DDM in the second dimension to dissociate the

398   respirasomes, confirmed the stability of the interaction between III_2 and IV within the respirasome

399   (Fig. S5F). Therefore, BNGE allows the isolation of the respirasome maintaining its structure to

400   perform functional studies, validating our functional observations.

401   **Superassembly of OXPHOS complexes influences the delivery of electrons and the**

402   **respiratory capacity within the electron transport chain.**

403   The lack of stability of the respiratory supercomplexes upon disruption of mitochondrial

404   membranes raises serious concerns on the interpretation of recent experiments where recombinant

405   AOX was added to a preparation of sub-mitochondrial particles (Fedor and Hirst, 2018). The data

406   obtained suggested that the interaction of CI and CIII in supercomplexes does not modify the

407   delivery of electrons to the alternative oxidase AOX by CoQ. These results led to the conclusion

408   that there is a unique CoQ pool equally accessible to CI and CII within mitochondrial inner

409   membrane. Given the observation that the native structure of supercomplexes is preserved in

410   intact mitochondria, we performed similar experiments but expressing AOX in the mitochondria

411   of different cell models: a) wild-type cells expressing AOX ($CIV^{WT}AOX$ and E9AOX); b) cells

412   lacking CIV which retain CI and $SCI+III_2$ superassembly due to the presence of AOX

413   ($CIV^{KO}AOX$); c) cells that lack CIII which preserve CI due to AOX expression but CI cannot

15

414   form supercomplexes with CIII (CIII^{KO}AOX). AOX expressed in mammalian mitochondria is

415   known to be functional and can recycle oxidized CoQ in cells lacking of mtDNA (Perales-

416   Clemente et al., 2008) or in cells lacking CIII or CIV (Guarás et al., 2016). We described

417   elsewhere that the expression of AOX prevent the degradation of CI in the absence of CIII or CIV

418   (Guarás et al., 2016) (Fig. S6A). We found that the level of AOX activity was similar between

419   the different cell lines (Fig. S6B). Following similar reasoning to that of Fan & Hirst, the delivery

420   of electrons from CI or CII to AOX should be independent of superassembly in the absence of

421   CIII. However, if the superassembly between CI and CIII has any effect on the activity of CI, in

422   the absence of CIV a change in the delivery of electrons from CI to AOX should be detected (Fig.

423   6A). In the two mutant cells we detected measurable CI-AOX and CII-AOX respirations, while

424   CIV-dependent respiration could not be recorded (Fig. 6B). Strikingly, CII-AOX dependent

425   respiration was insensitive to the presence of CIII, while CI-AOX dependent respiration was

426   significantly lower when CIII is present (Fig. 6B). This is true despite a higher NADH oxidation

427   capacity of CI in CIV^{KO}AOX cells (Fig. 6C). We also reasoned that if a CoQ pool was shared

428   between CII and CI, addition of succinate would outcompete with glutamate + malate-based AOX

429   respiration (Fig. 6D). We found that in either the wild type or in the CIV^{KO} cells, all expressing

430   AOX, the addition of succinate significantly increased the oxygen consumption over that

431   achieved by CI substrates (Fig. S6C, D and Fig. 6E). On the contrary, in CIII^{KO} AOX cells the

432   addition of succinate was unable to increase the AOX dependent oxygen consumption over that

433   reached by CI substrates (Fig.S6D and Fig. 6E). These results suggest that when CI is not

434   superassembled CoQ exist in a unique pool, whereas its superassembly triggers the formation of

435   two partially differentiated pools.

436   We then measured directly NADH or succinate dependent respiration (Fig. 6F, G) and

437   NADH oxidation (Fig. 6H) in mitochondrial membranes permeabilized by freeze & thawing in a

438   period of 4 min to prevent disruption of supercomplexes, and isolating mitochondria from wild

439   type, CIV^{KO} and CIII^{KO} cell models, all expressing AOX. This analysis offered a number of

440   interesting observations: (i) In the presence of CIII none of the substrates (NADH or succinate)

441   was able to reach the oxygen consumption levels obtained when both substrates were added

16

442 simultaneously (Fig 6F, G). This indicates that the delivery pathway of electrons to CoQ and

443 AOX is partially different for each substrate. (ii) NADH oxidation of the two wild-type cells lines

444 is different, being the E9 nuclear background significantly lower (≈50%) (Fig. 6H). We described

445 elsewhere that this is due to the presence of a missense mutation in COI that reduce the activity

446 of CIV, and hence, respiration (Acin-Perez, 2003), a fact that can also be observed in ED Fig.5C

447 and D. (iii) The addition of succinate did not impact on the oxidation of NADH in any wild type

448 cell line while the inhibition of CIV by KCN almost completely abolished it in wild type cells

449 (Fig. 6H). (iv) The ablation of CIV dramatically reduced the rate of oxidation of NADH to levels

450 equivalent to those caused by KCN (Fig. 6H). (iv) The ablation of CIII significantly increased the

451 NADH oxidation with respect to the levels of their isogenic wild type cells -which harbor a

452 mutation in COI- (Fig. 6H). This result parallels what we have observed measuring oxygen

453 consumption in intact mitochondria (Fig. S6D), and fully confirms that the dependence of CIV

454 activity limits the NADH oxidation capacity in E9 derived cells. (v) In the absence of CIII but not

455 of CIV, the addition of succinate significantly reduced the NADH oxidation, which in these cells

456 is fully dependent of AOX (Fig. 6H). All these results demonstrate that the superassembly of CI

457 with CIII, either in SCs or in the respirasome, impacts dramatically in the NADH oxidation

458 capacity of CI by modifying the delivery of electrons to CIV or AOX. Moreover, they indicate

459 that CI and CII can potentially outcompete for delivering electrons to AOX, a phenomenon that

460 is minimized by the presence of CIII. Our results with AOX expression substantially disagree

461 with those published by Fedor and Hirst (Fedor and Hirst, 2018). The reason for this discrepancy

462 is likely due to the unnoticed disruption of the supercomplexes under their experimental set up,

463 as explained above.

464 There are, however, additional experimental differences between our analyses that may

465 contribute to those discrepancies. Fedor et al. utilized mitochondria extracted from hearts as

466 starting material for their experiments (Fedor and Hirst, 2018). In order to minimize the impact

467 of the mitochondrial source, we generated a novel mouse model expressing AOX in the heart and

468 muscle mitochondria (see material and methods for details) and repeated the experiments with

469 purified wild type muscle and heart mitochondria expressing AOX. We first performed the

470   analysis of respiration in intact mitochondria fed with CI substrates (Glut+Mal) and assessing the

471   distribution of electrons either to CIV or AOX by using specific inhibitors for each enzyme (Fig.

472   6I, left panel). As expected, more than 70% of CI-dependent respiration was sensitive to CIV

473   inhibition, with a significant respiration mediated by AOX (Fig. 6I, left panel). We confirmed

474   that this assay was specific for CI by monitoring NADH oxidation in intact mitochondria by

475   measuring changes in NADH auto-fluorescence during the assay in the absence or in the presence

476   of rotenone (Fig. 6I, right panel). We additionally performed experiments in freeze-thawed

477   mitochondria prepared from hearts expressing AOX and confirmed again that NADH-linked

478   respiration was completely inhibited by KCN, whereas CII-AOX respiration was maintained (Fig.

479   S6E). Monitoring NADH absorbance allowed us to confirm that KCN completely abolished

480   NADH oxidation, in contrast to SHAM, which did not have any significant effect (Fig. S6F).

481   Similar results were obtained with mitochondrial preparations from muscle expressing AOX (Fig.

482   S6G, H). In conclusion, our results based on AOX expression could be reproduced using different

483   sources of mitochondria and demonstrate that CI supercomplex assembly affects the delivery of

484   electrons to AOX.

485   **Discussion**

486   In this report we provide strong experimental support demonstrating that the

487   superassembly of respiratory complexes into supercomplexes induce novel characteristics that

488   deeply impact on the structure, kinetics and efficiency of the respiratory chain. We demonstrate

489   it using isolated supercomplexes, mitochondrial preparations and cell cultures, and also using

490   animal models. We also provide experimental data that explains why previously published results

491   apparently contradict the main conclusion of this paper.

492   The main findings supporting our conclusion can be summarized as follows: 1) The

493   absence of functional SCAF1 in mice causes a reduction in exercise performance both in males

494   and females and compromise growth under food restriction in males. 2) The absence of functional

495   SCAF1 eliminates the physical interaction between CIII and CIV in the SC III_2+IV or within the

496   respirasome (I+III_2+IV). 3) In the absence of functional SCAF1, the respirasome can be

497   assembled in some tissues despite the fact that the direct interaction between CIII and CIV is

498 absent. 4) The absence of SCAF1 destabilizes the respirasome, reduces both oxygen consumption

499 and NADH oxidation and increases ROS production. 5) The interaction between CI and CIII

500 decreases the rates of NADH oxidation and respiration by AOX, implying the existence of a

501 partially segmented CoQ pool driven by the superassembly of CI and CIII.

502 Overall, the more relevant conclusion of our work is that the formation of respiratory

503 supercomplexes modify the kinetics and the flux of electrons occurring with non-superassembled

504 complexes. In one side, the role of SCAF1 in the respirasome becomes now clear. After strong

505 discrepancies, there is a general consensus that SCAF1 is required for the superassembly of

506 SC:III$_2$+IV and to provide stability to the respirasome (Cogliati et al., 2016; Lobo-Jarne et al.,

507 2018). There is also agreement in that SCAF1 function is lost in the mutated form of SCAF1 that

508 naturally arise in the C57BL/6 sub-strains (Enríquez, 2019; Lapuente-Brun et al., 2013). In spite

509 of that, BL6 heart mitochondria still assemble bona-fide respirasomes, which are structurally

510 different, less stable and functionally impaired. These findings clarify the role of SCAF1 in the

511 respirasome and the relevance of the interaction between CIII and CIV. On the other side, the

512 expression of AOX in cells and in mice and the ability to genetically control the free or

513 superassembled status of CI, allowed us to confirm that the delivery of electrons from CI but not

514 CII to AOX or CIV is asymmetric only if the formation of supercomplex I+III$_2$ is occurring. These

515 results confirm that superassembly of CI and CIII allow a partially segregation of the CoQ pool.

516 Interestingly, a very recent paper from the group of Sazanov studying the kinetic properties of

517 NADH to Cyt c electron transfer of the isolated supercomplex I+III$_2$ also found that CoQ trapping

518 within isolated respiratory supercomplex I+III$_2$ limits CI turnover (Letts et al., 2019).

519 In addition to the major findings, we exhaustive re-evaluated the mitochondrial BNGE

520 profiles from a variety of murine sources and analyzed the stability of the sample under several

521 conditions using advanced data-independent proteomics. This analysis provided relevant new

522 knowledge to better interpret BNGE analysis. In one hand, the Blue-DiS technology allowed us

523 to confirm, from a true hypothesis-free perspective, the presence, composition and stoichiometry

524 of the OXPHOS CI, CIII, CIV and CV in free and superassembled forms. Thus, while the protein

525 composition of these complexes is maintained, the proportion of OXPHOS supercomplexes is

19

526   tissue-specific. Moreover we demonstrate that regardless of the different positions where the

527   respirasome migrate, it maintains a constant stoichiometry of $I+III_2+IV$, a result that is in full

528   agreement with the different cryo-electron-microscopy derived structures published to date (Gu

529   et al., 2016; Letts et al., 2016; Sousa et al., 2016; Wu et al., 2016). This estimation stresses the

530   necessity to correct the experimentally unsupported tendency to assume that the different bands

531   of the respirasome contain increasing amounts of complex IV and to define the band with the

532   faster migration rate as the $I+III_2+IV$ respirasome and those with a higher apparent molecular

533   weight as successive megacomplexes (Lobo-Jarne et al., 2018). It is advisable to restrict the use

534   of the term megacomplex to define the association between SCs (Guo et al., 2017). Nevertheless,

535   it is remarkable that the respirasome migrate persistently in multiple bands, a phenomenon that

536   require further investigation of the potential partners. The Blue-DiS analysis also confirmed, from

537   a completely unbiased perspective, that SCAF1 is the main assembly factor which is present in

538   SC containing CIII and CIV. On the other hand, we describe unequivocally the existence of novel

539   SCs: I+IV that co-migrate between the free CI and SC: $I+III_2$ and $I+IV_2$ that co-migrate with SC:

540    $I+III_2$; and the co-migration of CI with CIV in the area of the respirasomes. CI and CIV

541   associations could be predicted from the evidence obtained by cryo-electron-microscopy that the

542   interaction between CI and $CIII_2$ is independent from that between CI and CIV (Letts et al., 2016;

543   Sousa et al., 2016). SC $I+VI_2$ was however unexpected. This novel SC, as well as some of the

544   already known associations may represent true SCs or partially disassembled elements from larger

545   complexes. In any case, their characterization in the BNGE is of major relevance because they

546   can lead to inaccurate interpretations. This may be the case of the proposed novel fast migrating

547   respirasome $(I+III_2+IV)$ that comigrate with $I+III_2$, despite the different molecular weight, solely

548   based on the fact the CI, CIII and CIV co-migrate in the same band (Sun et al., 2016). The co-

549   migration of $I+III_2$ with $I+IV_2$ is a more plausible explanation, since they have a very similar MW.

550   The co-migration CI with CIV in the area of the respirasomes, well above SC: $I+III_2$, does not

551   contain IV dimers and the added molecular weight of CI and CIV does not justify its apparent

552   MW. The fact that 2D-BNGE/DDM splits CI and CIV suggest as the more plausible explanation

553   that this co-migration imply the presence of a SC I+IV that interact with an unknown partner.

554   This additional SC may again flaw our interpretation of the BNGE gels. Thus, when the gels are

555   performed with a steep gradient or short run (as it is the case of the more used pre-casted native

556   gels) the SCs I+III$_2$+IV (the faster migrating band) and this particular SC: (I+IV)* may overlap

557   (as a potential example see (Lobo-Jarne et al., 2018)) leading to the wrong interpretation solely

558   based on the position of CIV that this band correspond to a respirasome.

559   A third important discovery reported here is that the respirasome and the SC: III$_2$+IV, and

560   at less extent SC I+III$_2$, are unstable after disruption of the mitochondrial membranes even if

561   preserved at 4 ºC. This previously unnoticed phenomenon raises concerns in the interpretation of

562   experiments aimed to measure the proportion and function of SCs when mitochondrial membrane

563   integrity is not preserved. More strikingly, the loss of respirasome and SC: III$_2$+IV is paralleled

564   by the specific proteolytic processing of SCAF1 by calpain-1 that causes the processed form of

565   SCAF1 to migrate together with CIV. If this cleavage is physiologically relevant or not need to

566   be further investigated, but at this point it explains discrepant results in the literature that

567   considered that SCAF1 as a shorter protein that acts as a mere isoform of CIV (Zhang et al., 2016).

568   By the same token it may explain the unexpected presence of variable amounts of SCAF1

569   associated with free CIV. Our observation is also coherent with the description of two respirasome

570   structures by several groups (Letts et al., 2016; Sousa et al., 2016) that differ in the connection

571   between III$_2$ and IV that is either present (tight respirasome) or absent (loose respirasome). Our

572   finding also explains the reported conversion of the tight respirasome into the loose one with time

573   (Letts et al., 2016). Therefore, these observations largely clarify the investigation of the

574   functional role of the respiratory supercomplexes using BNGE.

575   In summary, in this report we show that superassembly between respiratory complexes

576   substantially enhances the respiratory capacity of the electron transport chain while minimizing

577   ROS production. Superassembly establishes a segmented CoQ pool through the association

578   between CI and CIII, while SCAF1 plays a critical role in the III$_2$+IV interaction affecting the

579   structure and kinetic properties of the respirasome. Hence, SCAF1 is a key factor in the regulation

580   of the energy metabolism, optimizing efficiency under high energy demands or restricted

581   availability of nutrients.

582 **Acknowledgments**

590 **Author contributions:**

591 EC, JV & JAE: conceived and designed the analysis, EC, ML-L, FG-M-M. and JS-C performed

592 the proteomic analysis. SC, AG, PH-A RA-P, YM and MC-A: performed the BNGE and the

593 respirasomes functional analysis. SC, MC-A, J.R.H and R.A.C performed the *in vivo* experiments.

594 EC, SC, ML-L, JV, PH-A, JV and JAE interpreted the results. EC, JV and JAE wrote the paper.

595 **References**

596 Acin-Perez, R. (2003). An intragenic suppressor in the cytochrome c oxidase I gene of mouse
597 mitochondrial DNA. Hum. Mol. Genet. *12*, 329–339.

598 Acín-Pérez, R., Fernández-Silva, P., Peleato, M.L.M.L.M.L., Pérez-Martos, A., and Enriquez,
599 J.A.J.A. (2008). Respiratory Active Mitochondrial Supercomplexes. Mol. Cell *32*, 529–539.

600 Bayona-Bafaluy, M.P.M.P., Movilla, N., Pérez-Martos, A., Fernández-Silva, P., and Enriquez,
601 J.A.J.A. (2008). Functional genetic analysis of the mammalian mitochondrial DNA encoded
602 peptides: A mutagenesis approach. Methods Mol. Biol. *457*, 379–390.

603 Bianchi, C., Genova, M.L., Parenti Castelli, G., and Lenaz, G. (2004). The Mitochondrial
604 Respiratory Chain Is Partially Organized in a Supercomplex Assembly. J. Biol. Chem. *279*,
605 36562–36569.

606 Blaza, J.N., Serreli, R., Jones, A.J.Y., Mohammed, K., and Hirst, J. (2014). Kinetic evidence
607 against partitioning of the ubiquinone pool and the catalytic relevance of respiratory-chain
608 supercomplexes. Proc. Natl. Acad. Sci. *111*, 15735–15740.

609 Calvo, S.E., Clauser, K.R., and Mootha, V.K. (2016). MitoCarta2.0: An updated inventory of
610 mammalian mitochondrial proteins. Nucleic Acids Res. *44*, D1251–D1257.

611 Cogliati, S., Calvo, E., Loureiro, M., Guaras, A.M.A.M.A.M., Nieto-Arellano, R., Garcia-
612 Poyatos, C., Ezkurdia, I., Mercader, N., Vázquez, J., and Enriquez, J.A.J.A. (2016). Mechanism
613 of super-assembly of respiratory complexes III and IV. Nature *539*, 579–582.

614 Diaz, F., Fukui, H., Garcia, S., and Moraes, C.T. (2006). Cytochrome c Oxidase Is Required for
615 the Assembly/Stability of Respiratory Complex I in Mouse Fibroblasts. Mol. Cell. Biol. *26*,
616 4872–4881.

617   Enríquez, J.A. (2019). Mind your mouse strain. Nat. Metab. *1*, 5–7.

618   Enríquez, J.A.J.A. (2016). Supramolecular Organization of Respiratory Complexes. Annu. Rev.
619   Physiol. *78*, 533–561.

620   Eubel, H., Jänsch, L., and Braun, H.-P. (2003). New Insights into the Respiratory Chain of Plant
621   Mitochondria. Supercomplexes and a Unique Composition of Complex II. Plant Physiol. *133*,
622   274–286.

623   Fedor, J.G., and Hirst, J. (2018). Mitochondrial Supercomplexes Do Not Enhance Catalysis by
624   Quinone Channeling. Cell Metab. *28*, 525-531.e4.

625   Garaude, J., Acín-Pérez, R., Martínez-Cano, S., Enamorado, M., Ugolini, M., Nistal-Villán, E.,
626   Hervás-Stubbs, S., Pelegrín, P., Sander, L.E.L.E., Enríquez, J.A.J.A.J.A., et al. (2016).
627   Mitochondrial respiratory-chain adaptations in macrophages contribute to antibacterial host
628   defense. Nat. Immunol. *17*, 1037–1045.

629   García-Poyatos, C., Cogliati, S., Calvo, E., Hernansanz-Agustín, P., Lagarrigue, S., Magni, R.,
630   Botos, M., Langa, X., Amati, F., Vázquez, J., et al. (2019). Respiratory supercomplexes provide
631   metabolic efficiency in zebrafish. BioRxiv *doi.org/10.1101/818286*.

632   Glytsou, C., Calvo, E., Cogliati, S., Mehrotra, A., Anastasia, I., Rigoni, G., Raimondi, A.,
633   Shintani, N., Loureiro, M., Vazquez, J., et al. (2016). Optic Atrophy 1 Is Epistatic to the Core
634   MICOS Component MIC60 in Mitochondrial Cristae Shape Control. Cell Rep. *17*, 3024–3034.

635   Greggio, C., Jha, P., Kulkarni, S.S., Lagarrigue, S., Broskey, N.T., Boutant, M., Wang, X.,
636   Conde Alonso, S., Ofori, E., Auwerx, J., et al. (2017). Enhanced Respiratory Chain
637   Supercomplex Formation in Response to Exercise in Human Skeletal Muscle. Cell Metab. *25*,
638   301–311.

639   Gu, J., Wu, M., Guo, R., Yan, K., Lei, J., Gao, N., and Yang, M. (2016). The architecture of the
640   mammalian respirasome. Nature *537*, 639–643.

641   Guarás, A., Perales-Clemente, E., Calvo, E., Acín-Pérez, R., Loureiro-Lopez, M., Pujol, C.,
642   Martínez-Carrascoso, I., Nuñez, E., García-Marqués, F., Rodríguez-Hernández, M.A.M.A., et
643   al. (2016). The CoQH2/CoQ Ratio Serves as a Sensor of Respiratory Chain Efficiency. Cell
644   Rep. *15*, 197–209.

645   Guo, R., Zong, S., Wu, M., Gu, J., and Yang, M. (2017). Architecture of Human Mitochondrial
646   Respiratory Megacomplex I2III2IV2. Cell *170*, 1247-1257.e12.

647   Huertas, J.R.R., Al Fazazi, S., Hidalgo-Gutierrez, A., López, L.C.C., and Casuso, R.A.A.
648   (2017). Antioxidant effect of exercise: Exploring the role of the mitochondrial complex I
649   superassembly. Redox Biol. *13*, 477–481.

650   Ishihama, Y. (2005). Proteomic LC–MS systems using nanoscale liquid chromatography with
651   tandem mass spectrometry. J. Chromatogr. A *1067*, 73–83.

652   Lapuente-Brun, E., Moreno-Loshuertos, R., Acín-Pérez, R., Latorre-Pellicer, A., Colás, C.,
653   Balsa, E., Perales-Clemente, E., Quirós, P.M.P.M., Calvo, E., Rodríguez-Hernández, M.A.A., et
654   al. (2013). Supercomplex assembly determines electron flux in the mitochondrial electron
655   transport chain. Science (80-.). *340*, 1567–1570.

656   Lenaz, G., and Genova, M.L. (2007). Kinetics of integrated electron transfer in the
657   mitochondrial respiratory chain: random collisions vs. solid state electron channeling. Am. J.
658   Physiol. Physiol. *292*, C1221–C1239.

659   Letts, J.A., Fiedorczuk, K., and Sazanov, L.A. (2016). The architecture of respiratory

660   supercomplexes. Nature *537*, 644–648.

661   Letts, J.A., Fiedorczuk, K., Degliesposti, G., Skehel, M., and Sazanov, L.A. (2019). Structures
662   of Respiratory Supercomplex I+III2 Reveal Functional and Conformational Crosstalk. Mol. Cell
663   *75*, 1131-1146.e6.

664   Lobo-Jarne, T., Nývltová, E., Pérez-Pérez, R., Timón-Gómez, A., Molinié, T., Choi, A.,
665   Mourier, A., Fontanesi, F., Ugalde, C., and Barrientos, A. (2018). Human COX7A2L Regulates
666   Complex III Biogenesis and Promotes Supercomplex Organization Remodeling without
667   Affecting Mitochondrial Bioenergetics. Cell Rep. *25*, 1786-1799.e4.

668   Lopez-Fabuel, I., Le Douce, J., Logan, A., James, A.M., Bonvento, G., Murphy, M.P., Almeida,
669   A., and Bolaños, J.P. (2016). Complex I assembly into supercomplexes determines differential
670   mitochondrial ROS production in neurons and astrocytes. Proc. Natl. Acad. Sci. *113*, 13063–
671   13068.

672   Maranzana, E., Barbero, G., Falasca, A.I., Lenaz, G., and Genova, M.L. (2013). Mitochondrial
673   Respiratory Supercomplex Association Limits Production of Reactive Oxygen Species from
674   Complex I. Antioxid. Redox Signal. *19*, 1469–1480.

675   Milenkovic, D., Blaza, J.N., Larsson, N.-G., and Hirst, J. (2017). The Enigma of the Respiratory
676   Chain Supercomplex. Cell Metab. *25*, 765–776.

677   Moreno-Loshuertos, R., Acín-Pérez, R., Fernández-Silva, P., Movilla, N., Pérez-Martos, A., De
678   Cordoba, S.R.S.R., Gallardo, M.E.E., and Enríquez, J.A.J.A. (2006). Differences in reactive
679   oxygen species production explain the phenotypes associated with common mouse
680   mitochondrial DNA variants. Nat. Genet. *38*, 1261–1268.

681   Navarro, P., and Vázquez, J. (2009). A Refined Method To Calculate False Discovery Rates for
682   Peptide Identification Using Decoy Databases. J. Proteome Res. *8*, 1792–1796.

683   Perales-Clemente, E., Bayona-Bafaluy, M.P.P., Pérez-Martos, A., Barrientos, A., Fernández-
684   Silva, P., Enriquez, J.A.A., Perez-Martos, A., Barrientos, A., Fernandez-Silva, P., and Enriquez,
685   J.A.A. (2008). Restoration of electron transport without proton pumping in mammalian
686   mitochondria. Proc. Natl. Acad. Sci. *105*, 18735–18739.

687   Perales-Clemente, E., Fernández-Vizarra, E., Acín-Pérez, R., Movilla, N., Bayona-Bafaluy,
688   M.P.M.P., Moreno-Loshuertos, R., Pérez-Martos, A., Fernández-Silva, P., Enríquez, J.A.J.A.,
689   Fernández-Vizarra, E., et al. (2010). Five entry points of the mitochondrially encoded subunits
690   in mammalian complex I assembly. Mol. Cell. Biol. *30*, 3038–3047.

691   Quintana-Cabrera, R., Quirin, C., Glytsou, C., Corrado, M., Urbani, A., Pellattiero, A., Calvo,
692   E., Vázquez, J., Enríquez, J.A., Gerle, C., et al. (2018). The cristae modulator Optic atrophy 1
693   requires mitochondrial ATP synthase oligomers to safeguard mitochondrial function. Nat.
694   Commun. *9*, 3399.

695   Schagger, H. (2000). Supercomplexes in the respiratory chains of yeast and mammalian
696   mitochondria. EMBO J. *19*, 1777–1783.

697   Schägger, H. (2002). Respiratory chain supercomplexes of mitochondria and bacteria. Biochim.
698   Biophys. Acta - Bioenerg. *1555*, 154–159.

699   Sousa, J.S., Mills, D.J., Vonck, J., and Kühlbrandt, W. (2016). Functional asymmetry and
700   electron flow in the bovine respirasome. Elife *5*, 1–17.

701   Sun, D., Li, B., Qiu, R., Fang, H., and Lyu, J. (2016). Cell Type-Specific Modulation of
702   Respiratory Chain Supercomplex Organization. Int. J. Mol. Sci. *17*, 926.

703 Della Torre, S., Mitro, N., Meda, C., Lolli, F., Pedretti, S., Barcella, M., Ottobrini, L., Metzger,
704 D., Caruso, D., and Maggi, A. (2018). Short-Term Fasting Reveals Amino Acid Metabolism as
705 a Major Sex-Discriminating Factor in the Liver. Cell Metab. *28*, 256-267.e5.

706 Wittig, I., Braun, H.P., and Schägger, H. (2006). Blue native PAGE. Nat. Protoc. *1*, 418–428.

707 Wu, M., Gu, J., Guo, R., Huang, Y., and Yang, M. (2016). Structure of Mammalian Respiratory
708 Supercomplex I1III2IV1. Cell *167*, 1598-1609.e10.

709 Zhang, K., Wang, G., Zhang, X., Hüttemann, P.P., Qiu, Y., Liu, J., Mitchell, A., Lee, I., Zhang,
710 C., Lee, J., et al. (2016). COX7AR is a Stress-inducible Mitochondrial COX Subunit that
711 Promotes Breast Cancer Malignancy. Sci. Rep. *6*, 31742.

712 **Figure Legends**

713 **Figure 1. SCAF1 deficiency induces a conspicuous phenotype in mice. A,** BNGE

714 followed by western-blot showing the absence or presence of SCAF1 in the indicated

715 tissue and mouse strain. 113: C57BL/6JOlaHsd mice with the functional version of

716 SCAF1; 111: C57BL/6JOlaHsd mice (it harbors a non-functional version of SCAF1); KO

717 C57BL/6JOlaHsd mice without SCAF1. **B,** Scheme of the food restriction experiment

718 analyzed in **C**. **D,** Effect of SCAF1 on the maximum speed running in a treadmill by the

719 indicated mouse groups.

720 **Figure 2. Blue-DiS evidence of the formation of OXPHOS supercomplexes. A,** For each

721 complex, the number of protein PSMs was plotted against normalized protein abundances (see

722 Methods), showing that the relative proportions of proteins from CI (blue points), CIII (red points)

723 and/or CIV (green points) are constant in specific BNGE slices from liver mitochondria indicating

724 the presence of multimeric structures. Slices 2-4 correspond to a ternary structure (I+III+IV),

725 slices 5-6 and 9-10 to binary structures (I+III and III+IV, respectively) and slices 8 and 15 to

726 monomeric forms (I and IV, respectively). **B,** Similar results are obtained in heart and brain

727 mitochondria; for simplicity only one slice with the tertiary structure is shown. **C,** Cross-

728 correlation analysis of abundances of proteins forming part of each one of the supercomplexes,

729 showing that their relative proportions are tightly maintained across the consecutive slices. **D,**

730 Cross-correlation analysis of abundances of proteins of the indicated supercomplexes across the

731 four mitochondrial types, showing that their relative proportions are also constant independently

732 of the mitochondrial origin. **E,** Normalized profiles of CI, CIII and CIV from heart mitochondria

733   (black line) (see Methods) can be accurately explained as a superimposition (dashed thick red

734   line) of six gaussian peaks corresponding to monomeric and multimeric structures, as indicated.

735   The gaussian deconvolution was performed in a hypothesis-free manner by a simultaneous least-

736   squares fitting of the three normalized profiles adjusting the position, width and height of each

737   peak (thin lines) without any numeric constraint. In the case of CIV two additional peaks (CIV_2

738   and CIVm) had to be added to the model in order to explain the normalized profile (arrows). **F,**

739   Gaussian components used to model the normalized profiles of the four mitochondrial types. For

740   simplicity, the two multimeric CIV structures are not represented.

741   **Figure 3. Structural consequences of SCAF1-deficiency in the formation of SCs**. **A,**

742   2DBNGE (Dig/DDM) analysis of heart mitochondria resolving complexes and supercomplexes

743   in the first dimension and disrupting SCs into their component complexes in the second

744   dimension. NDUFA9 immunodetection in red indicate the migration of CI, COI immunodetection

745   in red indicate migration of CIV and CORE2 immunodetection in green indicate migration of

746   CIII. **B,** Gaussian deconvolution of the normalized profiles of heart and liver mitochondria from

747   BL6 mice, where the function of SCAF1 protein is impaired. Red asterisks indicate the position

748   of SC III_2+IV, which is completely absent in both tissues, and of the respirasome, which is absent

749   in the liver but remains detectable in the heart. **C,** 2DBNGE (Dig/DDM) resolving complexes and

750   supercomplexes in the first dimension and disrupting SCs into their component complexes in the

751   second dimension. Samples from BL6, CD1 and $BL6:S^{113}$ heart are compared highlighting the

752   area of migration of respirasomes, with the different traces at the bottom. Red asterisk indicates

753   absence of the respirasome-derived III_2+IV only in the BL6 sample indicating that III_2+IV are not

754   physically linked in SCAF1-deficient respirasomes. NDUFA9 immunodetection in red indicates

755   the migration of CI, COI immunodetection in red indicate migration of CIV and CORE2

756   immunodetection in green indicate migration of CIII. **D,** representation of the two structurally

757   different respirasomes.

758   **Figure 4. Functional consequences of SCAF1-deficiency in the activity of the respirasome.**

759   **A,** Scheme representing the experimental set up to analyze the function of the respirasomes. **B,**

760   Representative oxygen consumption traces obtained with heart respirasomes excised from the

761 BNGE and derived from either C57BL/6 or CD1 animals. The addition of different components

762 is indicated. **C & D,** NADH-dependent respiration rate normalized by TMPD-respiration rate (**C**),

763 or by mg. of protein (**D**) of heart respirasomes excised from BNGE from the indicated mouse

764 strain and measured in a Clark oxygen electrode. **e,** NADH oxidation rate by heart respirasomes

765 eluted from BNGE excised bands of the indicated mouse strain and measured by

766 spectrophotometry. **F & G,** Representative traces (**F**) and quantitative data (**G**) of H_2O_2

767 production upon NADH oxidation (upper-panel) or $CoQH_2$ oxidation (lower panel) by heart

768 respirasomes eluted from BNGE excised bands of the indicated mouse strain and estimated by

769 Amplex Red. When $CoQH_2$ oxidation was assayed rotenone was included to prevent the

770 interaction of $CoQH_2$ with CI, and the assay was performed.

771 **Figure 5. Supercomplexes are unstable upon mitochondrial membrane disruption. A,** BNGE

772 resolving complexes and SCs from CD1 liver from intact or digitonized mitochondria

773 preincubated during the indicated time at 4 ºC, and probed with the indicated antibody. **B,** BNGE

774 resolving complexes and SCs from CD1 liver from digitonized mitochondria preincubated during

775 the indicated time at 4 ºC, and probed with the indicated antibody. **C,** 2D-BNGE/PAGE resolving

776 complexes and SCs in the 1st dimension and protein components in the 2nd dimension from CD1

777 liver digitonized preparation preincubated 72 h at 4 ºC showing that SCAF1 is processed

778 (SCAF1*). The membrane was immunoblotted with the indicated antibodies. **D,** Structure of

779 SCAF1 sequence, mapping CIII- (in green), and CIV- (in yellow) interacting regions. The

780 predicted calpain-1 processing site is indicated with a blue line. **E,** Quantitative analysis of the

781 SCAF1-derived tryptic (LTSSVTAYDYSGK, in blue), and calpain 1-processed

782 (SSVTAYDYSGK, in orange) peptides. Both peptides were quantified in the BNGE slices

783 corresponding to SCs I+III$_2$+IV and III$_2$+IV and to IV$_2$, and to CIV in fresh or in 4ºC-incubated

784 liver mitochondria-enriched fractions. The calpain 1-processed peptide was only detected in the

785 non-fresh preparations, attached to CIV and IV$_2$ and also to the respirasome. A structural

786 interpretation of these results is presented at the left; the blue and orange shadows indicate

787 whether the SCAF1 peptide is tryptic or processed, respectively. **F,** 2D BNGE/PAGE showing

788 that the proteolytic cleavage of SCAF1 can be prevented by inhibition of Calpain-1. **G,**

27

789   BNGE/PAGE analysis of liver mitochondria showing that the stability of the respirasome and the

790   SC III2+IV is preserved after digitonization in the presence of a calpain-1 inhibitor. **H,** BNGE

791   profile for CIV (COI-red) and SCAF1 (green) in heart samples maintained at 4ºC after

792   digitonization during the indicated time.

793   **Figure 6. The superassembly between complexes I and III modulates the activity of CI and**

794   **functionally segments the CoQ pool. A,** Scheme representing the differential flux of electrons

795   to AOX from the indicated mutant cell line. **B,** Impact of the presence of CIII in the delivery of

796   electrons from CI and CII to AOX. **C,** DPI sensitive NADH oxidation capacity of the

797   mitochondrial preparation from the indicated cell line. **D,** Scheme representing the simultaneous

798   flux of electrons form either CI or CII to AOX from the indicated mutant cell line. **E,** Estimation

799   of the impact of the simultaneous addition of substrates for CII (succinate) on the CI-dependent

800   respiration with CI substrates (glutamate and malate) in the presence or absence of CIII. **F,** Impact

801   of CIII and CIV superassembly on the maximum respiration capacity with CII (succinate) or CI

802   (glutamate and malate) substrates vs. both substrates addsed simultaneously. **G**, Proportion of the

803   maximum respiration archivable by CI substrates in the presence or absence of CI and CIII

804   superassembly. **H,** Analysis of the flux of electrons from NADH and CI or succinate and CII to

805   AOX in the indicated freeze-thaw mitochondrial from wild type cells or mutant cells lacking CIV

806   or CIII all expressing AOX. **I,** Flux of electrons from NADH and CI to AOX or CIV in intact

807   heart mitochondria expressing AOX and monitored by oxygen consumption (left panel) or

808   autofluorescence of NADH (right panel).

809

810

811   **STAR METHODS**

812   **LEAD CONTACT AND MATERIALS AVAILABILITY**

813   Request of information and material should be made to José Antonio Enriquez. Mouse and cell

814   lines generated in this study are available upon request for a non-commercial use under a Material

815   Transfer agreement.

816   **EXPERIMENTAL MODEL AND SUBJECT DETAILS**

817   **Experimental Models** This study used mouse and cellular models which were generated in out

818   laboratory.

819   *Mouse generation: 1)* C57BL/6JOlaHsd mice with the functional version of SCAF1 were

820   generated as previously described(Cogliati et al., 2016). C57BL/6JOlaHsd mice knock out for

821   SCAF1 were generated by microinjection of ES cells knock-out in the first alleles from EuMMCR

822   repository in a C57BL/6JOlaHsd blastocysts. Further, the blastocysts were implanted in a pseudo

823   pregnant female C57BL/6JOlaHsd. 2) AOX expressing mice were generated by *genOway* by

824   targeted insertion of the AOX cDNA within the Rosa26 locus via homologous recombination in

825   embryonic stem cells originally derived from a 129 strain of mouse and injected into C57BL/6J

826   blastocysts and then re-implanted into OF1 pseudo-pregnant, and allowed to develop to term.

827   After removal the neo cassette flanked by FLP sites, the selected knock-in animasl were then

828   sistematically backcrossed for more than 20 generations to C57BL/6JOlaHsd background. The

829   expression of the transgene is dependent upon the Cre recombinase mediated excision of a *Lox*P

830   flanked transcriptional "STOP" cassette upstream the AOX cDNA. For this study we induce the

831   expression of AOX in muscle and heart by breeding the AOX animals with expressing CRE under

832   the ACTA promoter.

833   *Mouse experimentation.* All animal procedures conformed to EU Directive 86/609/EEC and

834   Recommendation 2007/526/EC regarding the protection of animals used for experimental and

835   other scientific purposes, enforced in Spanish law under Real Decreto 1201/2005. Approval of

836   the different experimental protocols requires the estimation of the adequate sample size as well

837   as the definition of the randomization and blinding criteria. The mice were fed a standard chow

838   diet unless other food regime was required (5K67 LabDiet).

839   *Alternative fasting protocol*. Starting from weaning, mice undergo to 48h of fasting alternate

840   between 24h of controlled feeding (standard chow diet 5K67LabDiet Rod18-A; LASQCdiet) both

841   with free access to water for 40 days. The weight has been recorded at the end of feeding phase.

842   *Maximal incremental running test*. Mice was forced to run on a treadmill at 20º slope (LE8700

843   (76-0303), Treadmill Panlab, Harvard Apparatus). After a minute of acclimatization at 10 cm/s,

844   the speed was increased up to 16 cm/s for 5 minutes and further every 2 minutes by 3cm/s until

845   exhaustion, that was considered to reach when the mouse spent 3s in the back of the rack.

846   *Cellular Models:* All cell lines were grown in DMEM (GibcoBRL) supplemented with 5% FBS

847   (foetal bovine serum, Gibco BRL). mtDNA-less mouse cells were generated by long term growth

848   of L929 mouse cell line (ATCC CCL-1) in the presence of high concentrations of Ethidium

849   Bromide (EthBr) as previously described(Acin-Perez, 2003). Control cells (control cells) were

850   generated by transformation of ρº929neo cells by cytoplast fusion using NIH3T3 fibroblasts as

851   mitochondrial donors(Bayona-Bafaluy et al., 2008).

852   **METHOD DETAILS**

853   *Blue-Native Gel Electrophoresis:* Supercomplex levels and compositions were analyzed in

854   isolated mitochondria from different tissues and cells by blue native electrophoresis

855   (BNGE)(Wittig et al., 2006). Mitochondrial proteins from heart tissue were solubilized with

856   10% digitonin (4g/g) (Sigma D5628) and run on a 3%–13% gradient Blue Native gel. The

857   gradient gel was prepared in 1.5 mm glass plates using a gradient former connected to a

858   peristaltic pump. After electrophoresis, the gels were further processed for proteomic

859   analysis, western blotting, 2D SDS-PAGE or 2D-BNGE (DDM) analysis. For 2D SDS-

860   PAGE, the first-dimension lanes were excised from the gel and incubated 1h at room

861   temperature in 1% SDS and 1% β-mercaptoethanol and run in a 16.5% second denaturing

862   gel. For 2D-BNGE (DDM) and 2D-BNGE Digitonin, first-dimension lanes were excised

863   from the gel and run in a 3-13% gradient gel in native condition adding 0.02% of DDM to

864   the cathode buffer.

865   ***Immunodetection of complexes and supercomplexes:*** After BNGE, 2DBNGE/DIG,

866   2DBNGE/DDM or 2DBNGE/PAGE, proteins were electroblotted onto PVDF transfer

867   membrane (Immobilon-FL, 0.45 µm, Merck millipore, IPFL00010) for 1 h at 100 V in

868   transfer buffer (48 mM Tris, 39 mM glycine, 20 % EtOH). A Mini Trans- Blot Cell system

869   (BioRad) was used. Sea Blocking buffer (Thermo Scientific 37527) or PBS with 5 % BSA

870   was used for 1 hour at room temperature (RT) to avoid non-specific binding of antibodies.

871   For protein detection, antibodies were incubated with the membrane for 2 hours at RT.

872   Secondary antibodies were incubated for 45 minutes at RT. The membrane was washed with

873   PBS 0.1 % Tween-20 for 5 minutes three times between primary and secondary antibodies

874   and after secondary antibodies, the last wash was only PBS. To study supercomplexes

875   assembly, the PVDF membrane was sequentially probed with antibodies Complex I (anti-

876   NDUFA9, Abcam ab14713), Complex IV (anti-COI. Invitrogen 35-8100), Complex III (anti-

877   core2, Proteintech), SCAF1 (anti-COX7A2L, St. John's laboratory STJ42268. This antibody

878   was generated by immunization of rabbit with KLH conjugated synthetic peptide between

879   37-65 amino acids from the central region of human COX7A2L. It recognizes an epitope in

880   the common part of full size and processed SCAF1, allowing to visualize the processed

881   SCAF1 migrated with CIV after Calpain processing as in Fig.5c and Fig.5f. This antibody

882   was discontinued and substituted by the anti-COX7A2L, St. John's laboratory STJ110597

883   produced with a full length recombinant human CoX7A2L that, in the same experimental

884   conditions does not recognize the calpain-1 processed SCAF1 that need to be identified only

885   by MS. Anti-MIC10 (MINOS1 Novusbio NBP1-91587) and anti-CHCHD3 (Proteintech

886   25625-1-AP).

31

887   ***Proteomics by data-independent scanning (DiS) mass spectrometry (MS).*** DiS is a data-

888   independent acquisition method that covers all possible fragmentations of precursors in the 400-

889   1100 m/z range in two LC-MS runs and has already been successfully used to study the

890   mitochondrial proteome(Cogliati et al., 2016; Glytsou et al., 2016; Quintana-Cabrera et al., 2018).

891   DiS uses narrow MS/MS windows of 2 m/z, typical of data-dependent acquisition methods,

892   allowing direct peptide identification by database searching and FDR control by using a

893   conventional target/decoy competition strategy, without requiring peptide fragmentation libraries.

894   The Blue-DiS workflow generated a permanent, multi-dimensional, high-resolution time-

895   fragment mass map for all possible precursors present in each BNGE fraction and each

896   mitochondrial sample, from which quantitative protein maps can be straightforwardly obtained

897   with minimal computation. BNGE gels were excised in 26 slices taking as reference some discrete

898   Coomassie stained bands: slice 6 corresponds to a band that mainly contains SC I + III$_2$, slice 10

899   to CV, slice 12 to free CIII$_2$, and slice 15 to free CIV. All slices were cut into cubes (2x2 mm),

900   reduced with 10mM DTT (GE Healthcare), alkylated with 55mM iodoacetamide (Sigma-Aldrich)

901   and subjected to a standard overnight in-gel digestion at 37ºC with 3 μg of sequencing grade

902   trypsin (Promega, Madison, WI, USA) in 100 mM ammonium bicarbonate, pH 7.8. After

903   desalting with C18 Omix cartridges (Agilent Technologies), the resulting tryptic peptide mixtures

904   were injected onto a C-18 reversed phase (RP) nano-column (75μm I.D. and 50 cm, Acclaim

905   PepMap, Thermo Fisher, San José, CA, USA) using an EASY-nLC 1000 liquid chromatography

906   system (Thermo Fisher, San José, CA, USA) and analysed in a continuous gradient consisting of

907   8–31% B for 130 min, 50–90% B for 1 min (B= 0.5% formic acid in acetonitrile). Peptides were

908   eluted from the RP nanocolumn at a flow rate of ∼200nl min^{-1} to an emitter nanospray needle for

909   real-time ionization and peptide fragmentation in either a Q-Exactive or a Q-Exactive HF mass

910   spectrometer (Thermo Fisher). Each sample was analysed in two chromatographic runs covering

911   different mass ranges (from 400 to 750 Da, and from 750 to 1,100 Da, respectively). The DiS

912   cycle consisted of 175 sequential HCD MS/MS fragmentation events with 2-Da windows that

913   covered the whole 350 Da range. HCD fragmentation was performed at 30 normalized collisional

914   energy, a resolution of 17,500 and a maximum injection time of 80 ms with the AGC set to a

32

915   target of 3×10^5 ions. The whole cycle lasted 30 s or less depending on ion intensity during

916   chromatography. Peptide identification was performed using Sequest running under Proteome

917   Discoverer 1.4 (Thermo Fisher Scientific), allowing two missed cleavages, and using 2 Da and

918   20 p.p.m. precursor and fragment mass tolerances, respectively. Met oxidation and Cys

919   carbamydomethylation were selected as dynamic and static modifications, respectively. FDR for

920   peptide identification was controlled using a separate inverted database and the refined

921   method(Navarro and Vázquez, 2009). Visualization, validation and quantification of MS/MS

922   spectra from specific peptides was performed using Vseq script, as described(Cogliati et al.,

923   2016).

924   **_Protein and complex profiling._** Quantitative protein migration profiles from Blue-DiS analyses

925   were obtained by spectral counting, summing up the number of peptide-spectrum matches (PSMs)

926   of all peptides identified for each protein on each slice of the gel. In the case of protein complexes,

927   the total PSMs of the proteins contained in the complex was used for quantification. The

928   normalized BNGE profile of each complex was constructed by calculating the slope from the plot

929   of protein PSMs in a given slice versus protein PSMs in a slice used as reference (the one with

930   the highest number of PSMs). The normalized abundance of each protein within a complex was

931   calculated as the slope from the plot of PSMs of the protein in the different slices versus the PSMs

932   of the most abundant protein from the complex in the same slices.

933   **_Determination of stoichiometry between complexes in SC._** We observed that the number of

934   PSMs for each protein, as calculated by DiS, was approximately proportional to the number of

935   tryptic peptides detectable by MS (NOP) (ED Fig. 3C, left). This finding agrees well with the use

936   of the "protein abundance index" by other authors, which normalizes spectral counts by the

937   number of detectable peptides(Ishihama, 2005). This consideration allowed us to calibrate the

938   individual MS response of each protein, generating an estimation of the effective NOP (ED Fig.

939   3C, right). By plotting, per each complex, the PSMs of the proteins against their effective NOP,

940   we could estimate from the slopes the molar stoichiometries of complexes within each slice (ED

941   Fig. 3d).

33

942 ***Activity of complexes or respirasomes from BNGE eluted bands.*** CD1, BL6:S[111] and BL6:S[113]

943 heart mitochondria were extracted, processed and run in BN-PAGE as described above. CI, CIII$_2$,

944 CIV-monomer or respirasome bands were quickly excised from gels and minced on ice. The grist

945 was immediately resuspended in Medium MAITE and respirasomes eluted by twirling for 4 hours

946 at 4ºC. Elution was collected and mixed with the appropriate volume of MAITE + 2.5 mg/ml

947 BSA at 37 ºC to reach 1 mL. Reaction was started by adding 100 μM NADH, 130 μM CoQ$_1$,

948 reduced DQ 130 μM, oxidized Cyt c 100 μM. NADH, oxidized CoQ$_1$ and Cyt c levels were

949 tracked by recording absorbance at 340 nm, 289 nm and 550 nm, respectively for 240 sec in a

950 UV/VISJASCO spectrophotometer. Optimal absorbance values were calculated by titration of

951 each reactive in MAITE + 2.5 mg/ml BSA. DQ maximal absorbance peak could not be estimated

952 due to the consequent turbidity of its dissolution in an aqueous environment. Baseline NADH

953 oxidation and CoQ$_1$ reduction from the same elution was recorded after addition of 1 μM

954 rotenone. Baseline Cyt c reduction from the same elution was recorded after addition of 2.5 μM

955 antimycin A. Baseline Cyt c oxidation from the same elution was recorded after addition of 1 mM

956 KCN.

957 ***Oxygen consumption by BNGE respirasome bands.*** CD1, BL6:S[111] and BL6:S[113] heart

958 mitochondria were extracted, processed and run in BN-PAGE as described above. CIV-monomer

959 or respirasome bands were quickly excised from gels and minced on ice. The grist was

960 immediately resuspended in MAITE + 2.5 mg/ml BSA at 37ºC and introduced in an Oxytherm

961 System S1/MINI. Reaction was started by adding 100 μM reduced Cyt c for CIV-monomer or

962 100 μM NADH for respirasomes. Oxygen levels were tracked for at least 180 seconds and

963 baseline oxygen consumption was recorded after addition of 1 mM KCN for CIV-monomer or 1

964 μM rotenone for respirasomes.

965 ***H$_2$O$_2$ production by respirasomes from BNGE eluted bands.*** CD1, BL6:S[111] and BL6:S[113] heart

966 mitochondria were extracted, processed and run in BN-PAGE as described above. Respirasome

967 bands were quickly excised from gels and minced on ice. The grist was immediately resuspended

968 in Medium MAITE and respirasomes eluted by twirling for 4 hours at 4ºC. Elution was collected

969 and mixed with Amplex Red solution (Molecular probes), following manufacturer's instructions.

970 Reaction was started by adding 100 µM NADH or 100 µM $CoQH_2$+1µM rotenone. Amplex Red

971 levels were tracked by recording fluorescence at 540/590 nm (exc/emm) for 2400 sec in a

972 Fluoroskan Ascent fluorimeter (Thermo Labsystems). Baseline Amplex Red fluorescence from

973 the same elution was recorded after addition of 5U/mL of SOD and Catalase.

974 ***NADH oxidation monitoring in intact mitochondria by autofluorescence.*** AOX expressing mice

975 heart mitochondria were extracted as described above and immediately resuspended in medium

976 MAITE at 4ºC. Mitochondria were mixed with the appropriate volume of MAITE+ 2.5 mg/ml

977 BSA at 37 ºC to reach 100 µl. Reaction was started by adding 5 mM Glu + 5 mM Mal ± 1 mM

978 KCN, 5 mM SHAM or ± 1 µM rotenone. NADH levels were tracked by recording

979 autofluorescence at excitation/emission of 340/475 nm for 20 min in a Fluoroskan Ascent

980 fluorimeter (Thermo Labsystems)

981 ***Oxygen consumption measurement.*** AOX expressing heart mitochondria of mitochondria from

982 AOX expressing cell lines were extracted as described above and immediately resuspended in

983 medium MAITE at 4ºC. To permeabilize mitochondrial membranes, mitochondria were subjected

984 to a freeze-thaw step. Intact or freeze-thawed mitochondria were mixed with the appropriate

985 volume of MAITE + 2.5 mg/ml BSA at 37 ºC and placed in an Oxytherm System S1/MINI.

986 Reaction was started by adding 5 mM Glu + 5 mM Mal ± 10 mM succinate ± 1 mM KCN, 5 mM

987 SHAM or ± 1 µM rotenone. Permeabilized mitochondria were provided with 100 µM NADH or

988 100 µM CoQ_1H_2. Baseline levels were recorded after addition of 1µM rotenone or 5 mM SHAM.

989 ***Activity of complexes in freeze-thaw mitochondria.*** AOX expressing heart mitochondria of

990 mitochondria from AOX expressing cell lines were extracted as described above. Mitochondria

991 were immediately resuspended in medium MAITE and subjected to a freeze-thaw step. Freeze-

992 thaw mitochondria were mixed with the appropriate volume of MAITE + 2.5 mg/ml BSA at 37

993 ºC to reach 1 mL. Reaction was started by adding 100 µM NADH and in some cases 1 mM

994 $Fe(CN)_6$, 1 µM rotenone + 1 µM antimycin A, 100 µM succinate or 1 mM KCN was added to the

35

995   reaction mixture. Since the accessibility of CoQ-analogs could be differential across the different

996   AOX-cell models (i.e. with or without supercomplexes), we performed DPI-sensitive

997   NADH:Fe(CN)$_6$ activity (i.e. an activity for FMN in CI) which allowed us to quantify CI-content.

998   NADH and Fe(CN)$_6$ levels were tracked by recording absorbance at 340 nm and 412 nm,

999   respectively for 240 sec in a UV/VISJASCO spectrophotometer. Baseline NADH consumption

1000   from the same sample was recorded after addition of 1 μM rotenone. Baseline Fe(CN)$_6$

1001   absorbance from the same sample was recorded after addition of 5 μM diphenyleneiodium (DPI).

1002   **QUANTIFICATION AND STATISTICAL ANALYSIS**

1003   ***Statistical analysis.*** Unless specified, statistical analyses and graphics were produced with

1004   GraphPad Prism 8 software. Data sets were compared by t-test, ANOVA or non-parametric

1005   analysis when corresponded and with p-values adjusted for multiple test. Differences were

1006   considered statistically significant at P values below 0.05. *$p\text{-}value < 0.05$; ** $p\text{-}value < 0.01$;

1007   *** $p\text{-}value < 0.001$; **** $p\text{-}value < 0.0001$. All results are presented as mean ± SD or mean ±

1008   SEM.

1009   **DATA AND CODE AVAILABILITY**

1010   Some of the datasets supporting the current study have not been deposited in a public repository

1011   yet, but will be done when possible, meanwhile they are available from the corresponding author
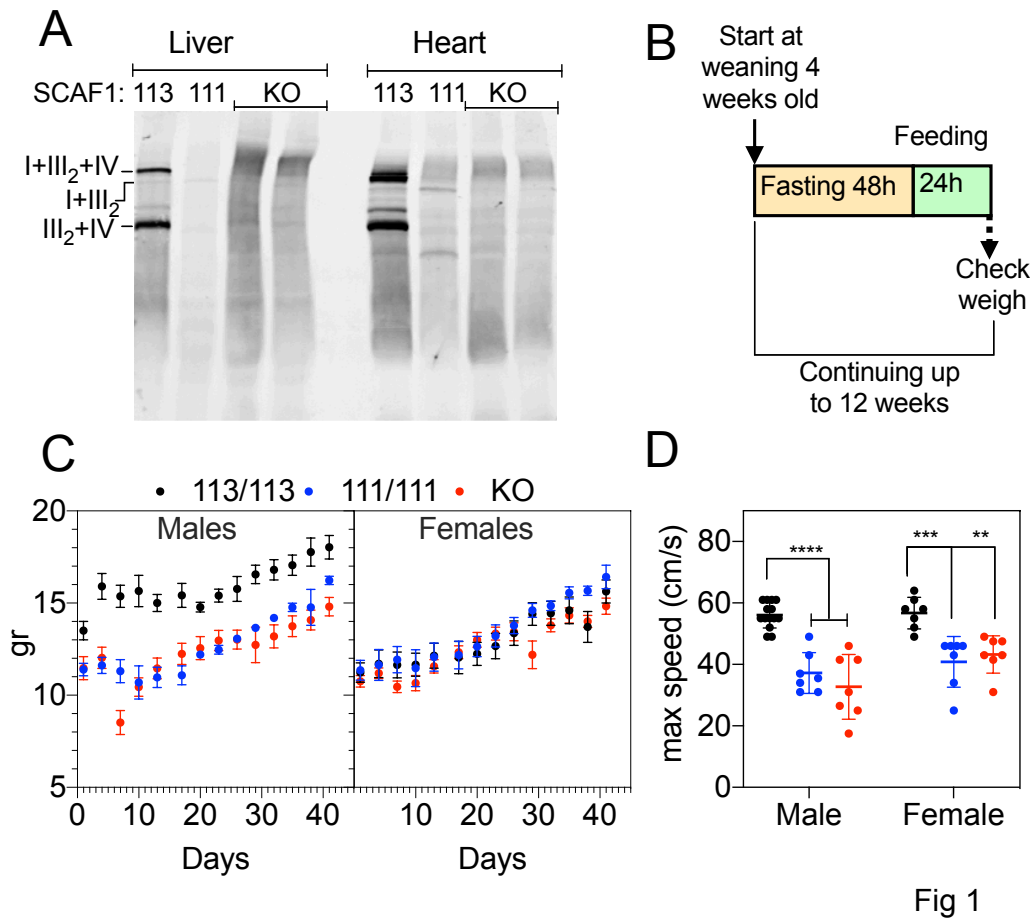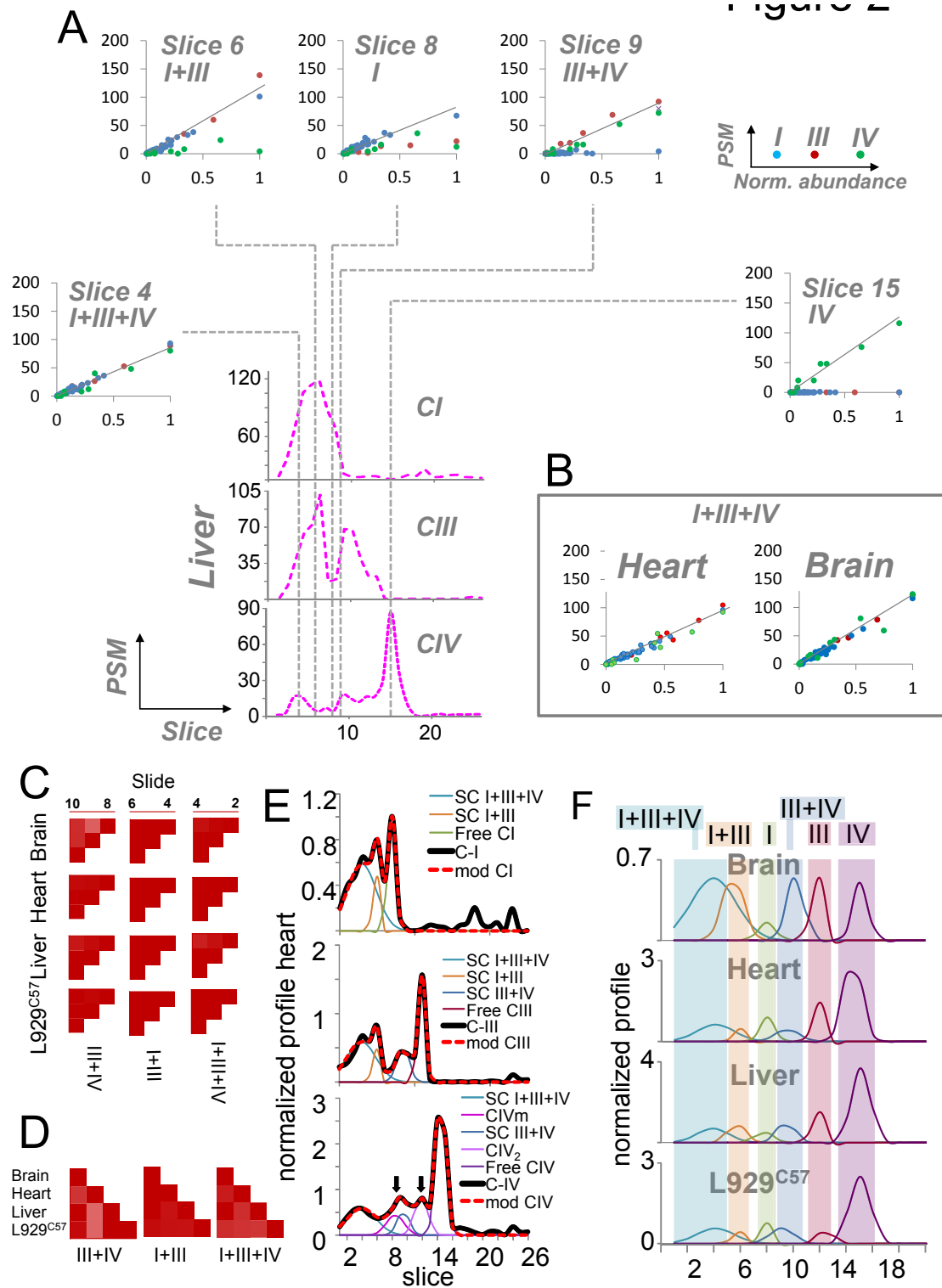
1012   on request.

1013

Fig 1

1014

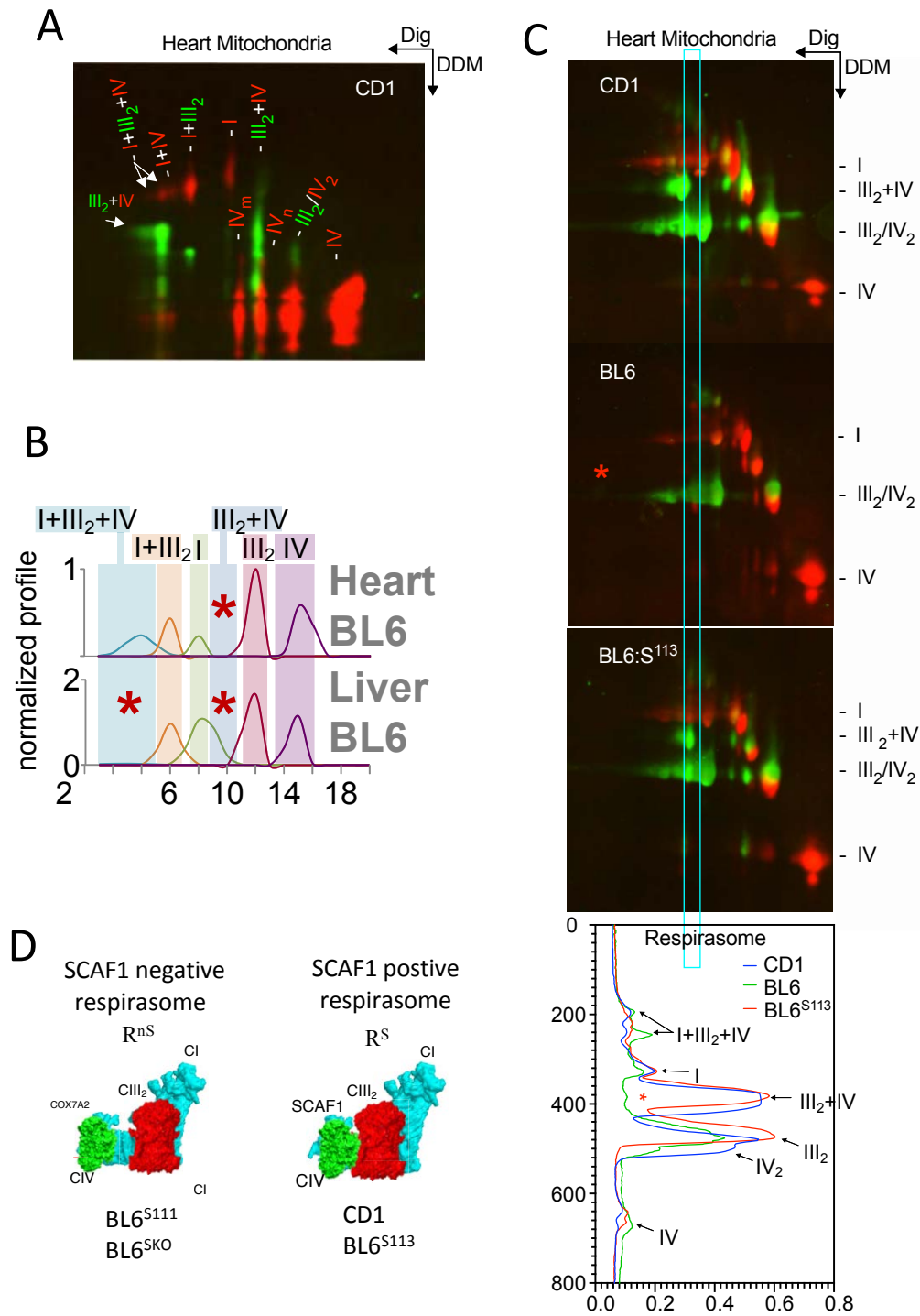**Figure 1. SCAF1 deficiency induces a conspicuous phenotype in mice.**

1016

1017

Figure 2. Blue-DiS evidence of the formation of OXPHOS supercomplexes.

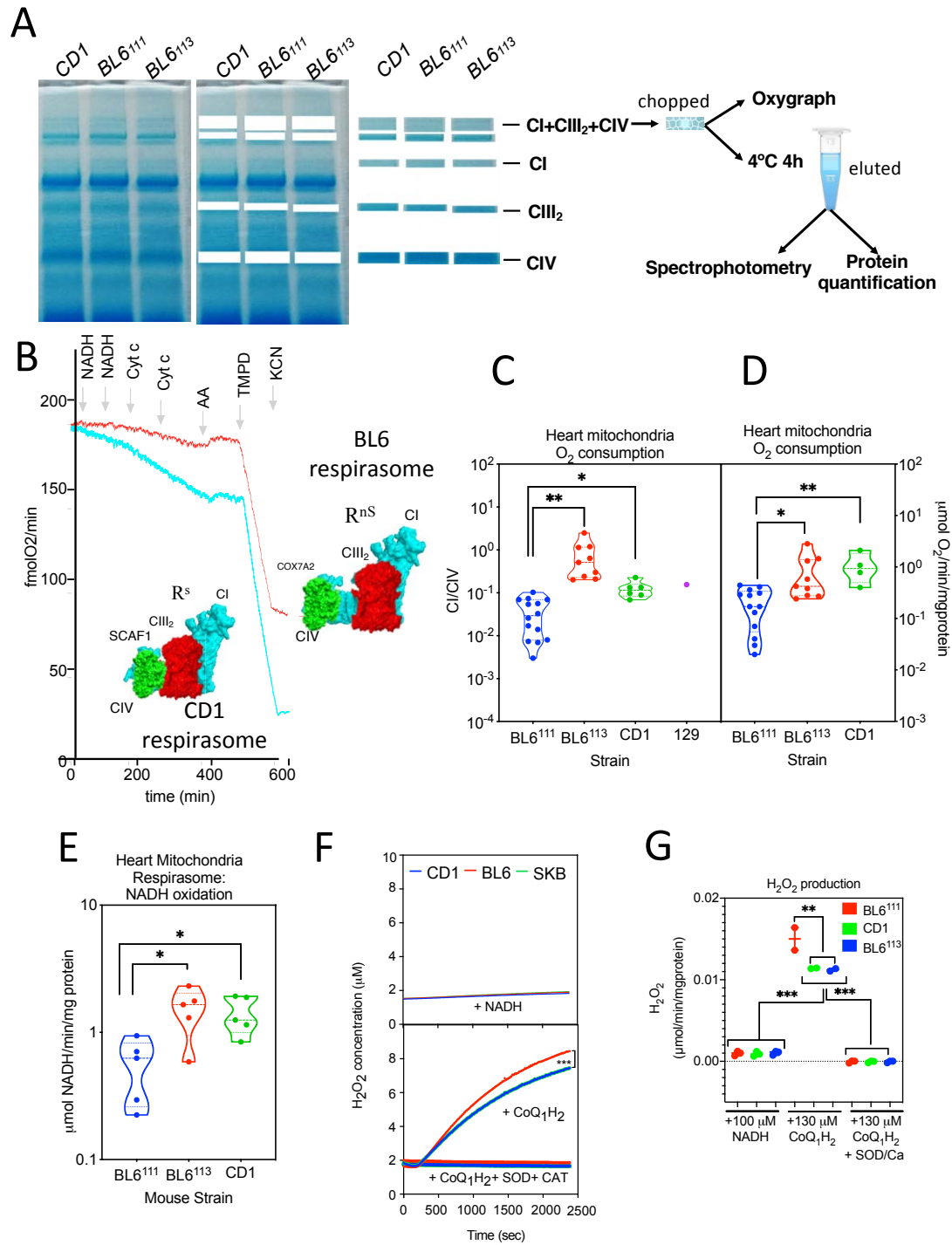1019

1020

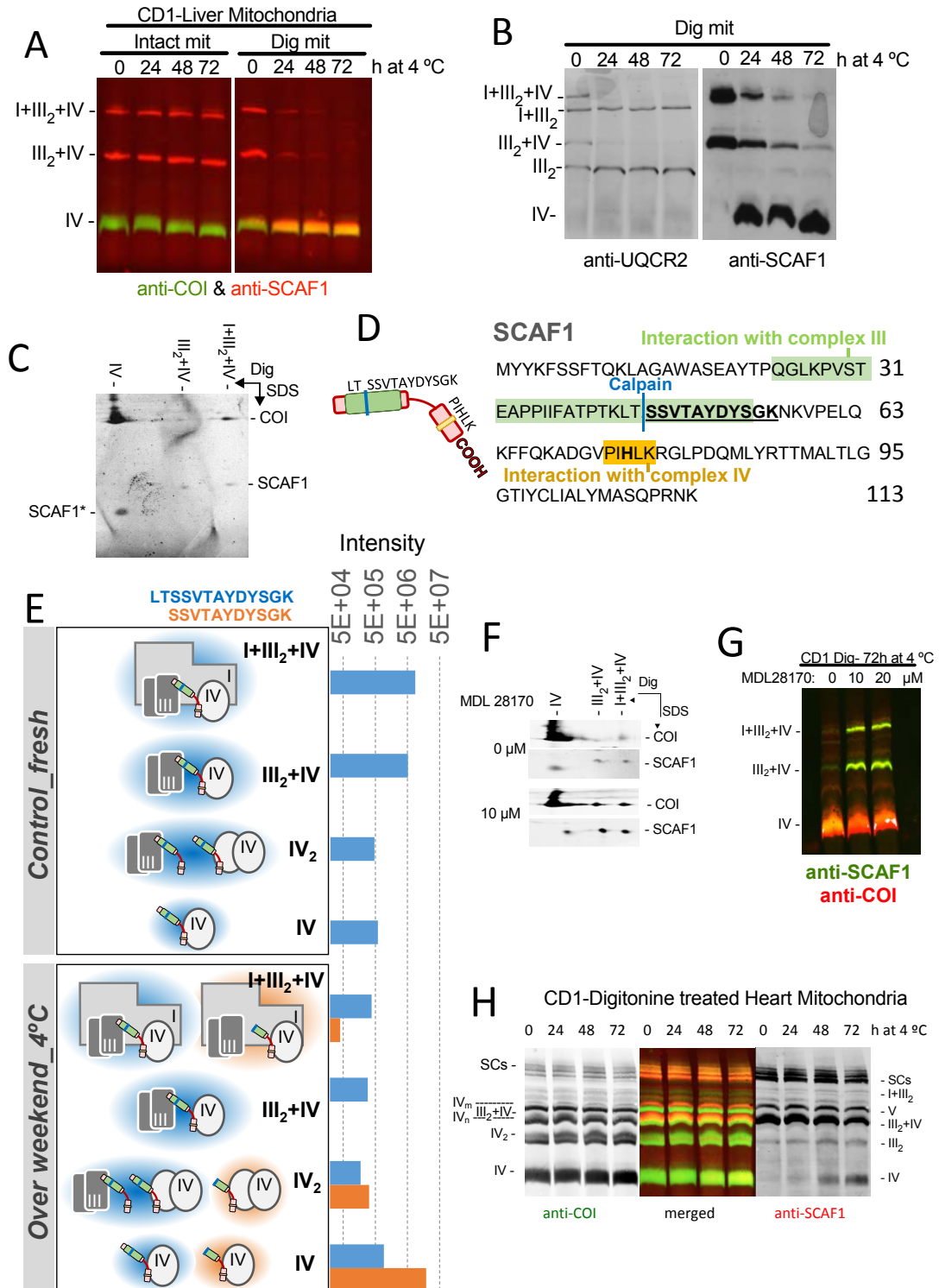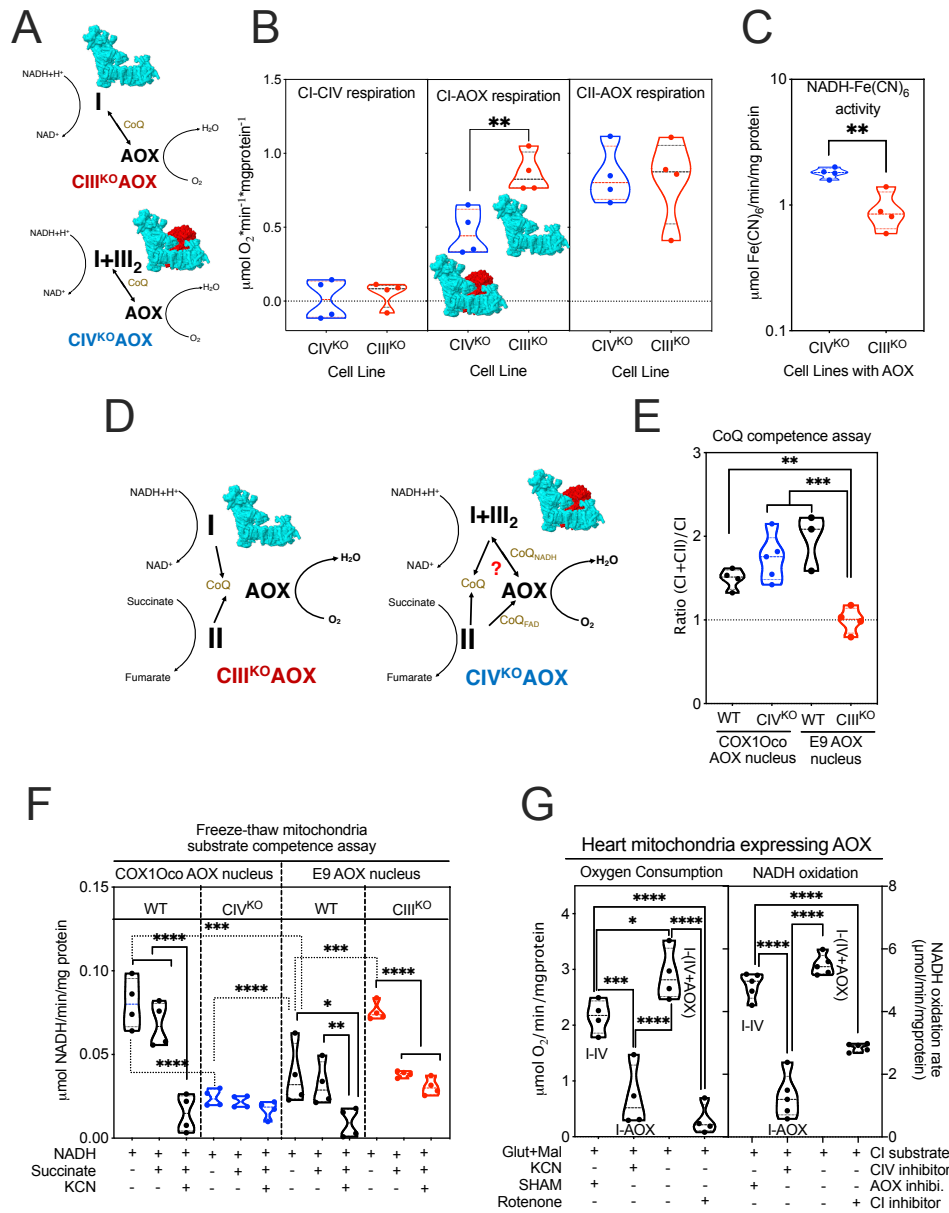**Figure 3. Structural consequences of SCAF1-deficiency in the formation of SCs.**

1022

1023

Figure 4. Functional consequences of SCAF1-deficiency in the activity of the respirasome.

1025

Figure 5. Supercomplexes are unstable upon mitochondrial membrane disruption.

1028

Figure 6. The superassembly between complexes I and III modulates the activity of CI and functionally segments the CoQ pool.